
Article:
Coyte, K.Z., Tabuteau, H., Gaffney, E.A. et al. (2 more authors) (2017) Microbial competition in porous environments can select against rapid biofilm growth. Proceedings of the National Academy of Sciences of the United States of America, 114 (2). E161-E170. ISSN 0027-8424

https://doi.org/10.1073/pnas.1525228113

Microbial competition in porous environments can select against rapid biofilm growth

Katharine Z. Coyte [*] [†] [‡] [§], **Hervé Tabuteau** [¶], **Eamonn A. Gaffney** [†], **Kevin R. Foster** [*] [‡], **and William M. Durham** [*] [‖]

[*]Department of Zoology, University of Oxford, United Kingdom,[†]Wolfson Centre for Mathematical Biology, University of Oxford, United Kingdom,[‡]Oxford Centre for Integrative Systems Biology, University of Oxford, United Kingdom,[§]Memorial Sloan Kettering Cancer Center, United States of America,[¶]Institut de Physique de Rennes, Université de Rennes 1, France, and [‖]Department of Physics and Astronomy, University of Sheffield, United Kingdom.

Submitted to Proceedings of the National Academy of Sciences of the United States of America

Microbes often live in dense communities called biofilms where competition between strains and species is fundamental to both evolution and community function. While biofilms are commonly found in soil-like porous environments, the study of microbial interactions has largely focused on biofilms growing on flat, planar surfaces. Here we use novel microfluidic experiments, mechanistic models, and game theory to study how porous media hydrodynamics can mediate competition between bacterial genotypes. Our experiments reveal a fundamental challenge faced by microbial strains that live in porous environments: cells that rapidly form biofilms tend to block their access to fluid flow and redirect resources to competitors. To understand how these dynamics influence the evolution of bacterial growth rates we couple a model of flow-biofilm interaction with a game theory analysis. This shows that hydrodynamic interactions between competing genotypes give rise to an evolutionarily stable growth rate that stands in stark contrast with that observed in typical laboratory experiments: cells within a biofilm can outcompete other genotypes by growing more slowly. Our work reveals that hydrodynamics can profoundly affect how bacteria compete and evolve in porous environments, the habitat where most bacteria live.

bacterial evolution | porous media flow | game theory | adaptive dynamics

Modern microbiology relies on growing cells in liquid cultures and agar plates. While these enable high throughput and repeatability, they lack the complex physical and chemical landscapes that microbes experience in their natural environments. This environmental heterogeneity is increasingly recognized to exert a powerful influence on microbial ecology across a wide diversity of habitats, ranging from the ocean to the human gut [1, 2, 3, 4]. While advances in sequencing technology now allow us to resolve how the genetic composition of microbial communities changes in response to environmental conditions [5, 6], we often lack a mechanistic understanding of the underlying processes. Novel empirical approaches, which simulate the conditions found in realistic microbial habitats, are needed to understand the strategies that cells use to gain an advantage over their competitors [7].

Most bacteria live in porous environments between the particles that compose soil, aquifers, and sediments, and these cumulatively comprise roughly half of the carbon within living organisms globally [8]. Cells in porous environments typically reside in surface attached structures known as biofilms [9], in which diverse bacterial genotypes live under intense competition for limited resources [10, 11]. Recent efforts have identified specialized mechanisms that cells use to gain advantage over competing genotypes in biofilms, ranging from the secretion of toxins, to polymer production, and metabolic regulation [12, 13, 14, 15, 16, 17, 18]. While genotypic competition is most frequently studied in biofilms growing on simple flat surfaces [19, 20, 21], biofilms growing in the interstitial spaces within porous structures face additional constraints. In porous environments space is much more limited, and biofilm growth tends to attenuate the fluid flow that supplies cells with nutrients and facilitates dispersal.

Biofilms typically reduce the flow through porous environments by orders of magnitude at the Darcy scale [22], a macroscopic scale that measures the flow averaged over many pore spaces. Harnessing this effect, biofilms can be used to limit the transport of pollutants that have leaked into groundwater aquifers and to facilitate the extraction of petroleum from recalcitrant regions of reservoirs [23, 24]. However, biofilm-induced clogging also generates unwanted effects: for example it severely limits the efficiency of porous filtration systems [25] and curtails the rate at which water infiltrates into aquifers, exacerbating droughts [26]. Due to its importance, the attenuation of flow by biofilms has long been studied at the Darcy scale [27, 28] and more recent works have sought to resolve how this is in turn mediated by biofilm-hydrodynamic interactions at the microscopic pore scale [29, 30, 31]. However, it is largely unknown how these interactions influence the ecology and evolution of the bacteria themselves. Here, we combine experiments and models to show that porous media hydrodynamics can dramatically affect the principles of bacterial competition and evolution.

Significance

The overwhelming majority of bacteria live in porous environments, like soil, aquifers, and sediments, where they facilitate many important processes. Despite this, we understand little about how these complex environments shape the composition of the microbial communities that live within them. Here we combine two diverse bodies of theory – fluid dynamics and game theory – to shed light on how bacteria evolve in these habitats. We show that bacteria in porous environments face a fundamental dilemma: they rely on flow for nutrients and dispersal, however, as cells grow, they tend to reduce their access to flow, diverting it instead to competitors. In contrast with classical theory, our results suggest that cells within a biofilm can obtain a competitive advantage by growing more slowly.

Reserved for Publication Footnotes

[0]To whom correspondence should be addressed: Email: kevin.foster@zoo.ox.ac.uk or w.m.durham@sheffield.ac.uk. K.Z.C., H.T. and W.M.D. designed and performed the microfluidic experiments; K.Z.C., E.A.G., K.R.F., and W.M.D. developed the mathematical models; and K.Z.C., E.A.G., K.R.F., and W.M.D. wrote the paper with input from all authors.

Results

A conceptual model to study hydrodynamic interactions between competing biofilms. Bacteria within biofilms tend to form patches of genetically-identical cells, even when the cells from which they are founded are initially mixed. This occurs because *in situ* growth, combined with the low mobility of cells within biofilms, means that clonemates tend to remain in close proximity to one another [32, 33]. Moreover, genotypic patchiness in biofilms is enhanced by population bottlenecks, which occur more frequently in nutrient limited conditions, and when biofilms are initiated from a sparse distribution of attached cells [34, 35, 36]. Based on these observations, we focus here on the competition between localized biofilm patches that are each comprised of a single genotype and assume that competing patches occupy different pore spaces.

To investigate how biofilm growth influences the flow through a porous environment we calculated the Stokes flow through a representative network of pore spaces that is driven by a difference in pressure at the boundaries (Fig. 1 *A*, *Materials and Methods*). The addition of a small impermeable biofilm 'patch' sharply reduces the flow through the pore in which the biofilm resides, while concurrently increasing the flow through neighboring pores (Fig. 1 *B, C*). While the magnitude of this flow diversion depends on the specific geometry of the pore space, this simulation shows that as a biofilm patch proliferates, it tends to decrease its access to flow, whilst increasing the flow to patches of biofilm that reside along other flow paths. This diversion of flow introduces a new way in which biofilms can interact: genotypes inhabiting a porous environment can affect one another via modulating their respective access to flow. This 'hydrodynamic interaction' differs from interactions observed in classical biofilm assays, where different genotypes growing together on flat surfaces typically have to be in close proximity to interact, for example through capturing one another's nutrients, or via cell secretions. Rather, here we see that in porous environments biofilms can influence one another over much larger distances, by either curtailing or increasing one another's ability to capture flow.

Though porous substrates harbor many biofilm patches that can simultaneously perturb one another's flow environment, we idealize this network of interactions as a collection of its constituent pairwise interactions. We then resolve the dynamics of competition between a single pair of biofilm patches, each of which is composed of a different genotype. In this pairwise approximation, the proportion of the total volumetric flow rate, Q_T, that passes each biofilm is a function of the hydrodynamic resistance of both its pore space and that of its competitor, which each are in turn a function of the thicknesses of the biofilms, k_1 and k_2 (Fig. 1 *D, E*). In this model the growth of a biofilm tends to decrease its access to flow and increase the flow past its competitor (Fig. 1 *F*). Importantly, our pairwise model captures the dynamics observed in our Stokes flow simulation, but is much more tractable and easily parameterized. Flow through a network of porous spaces can be modeled by fixing either the pressure gradient or the flow rate at the boundaries [37], with the former better characterizing flow through natural systems. However, localized biofilm growth in either of these scenarios will produce a flow diversion at the pore scale, as observed in our conceptual model.

Microfluidic experiments show that rapidly expanding biofilms tend to divert flow to biofilms that increase in thickness more slowly. We next developed a microfluidic version of our pairwise flow model to experimentally test how pore scale hydrodynamics affects the competition between genotypes that form biofilms at different rates (Fig. 2, Fig. S1). For this we chose a well-studied *Escherichia coli* experimental system. Specifically, we competed wild-type *E. coli* cells with $\Delta rpoS$ cells. The latter cells lack the ability to produce the sigma factor RpoS and, as a result, form biofilms at a much slower rate than the parental genotype (Figs. 2 *G*, S2, [38, 39]). The two genotypes were inoculated separately in either arm of the device, each of which represents a pore (Fig. 2 *A, B*). One of the pores was irrigated with media mixed with dye, while the other was irrigated with clear media, which allowed us to measure the relative proportion of flow passing through each pore by tracking the dye interface downstream of their juncture (see *Supporting Information*). Control experiments showed that neither the dye, nor the fluorescent proteins used to differentially label the strains, had an appreciable effect on biofilm formation (Fig. S2).

In porous environments biofilm growth is opposed by flow-induced detachment, which reduces the thickness of biofilms by shearing away cells from its surface [40, 41, 42]. To simulate different ambient flow conditions in our experiment, and thus the relative amount of detachment, we applied a total flow rate of either $Q_T = 0.1$ ml h^{-1} or $Q_T = 2$ ml h^{-1}. In the low flow treatment, the rapidly expanding wild-type biofilm increased its pore's hydrodynamic resistance and diverted flow to the neighboring pore space containing the $\Delta rpoS$ biofilm. The reduction in flow experienced by the wild-type biofilm further reduces its detachment, driving a positive feedback loop that ultimately ends with the $\Delta rpoS$ biofilm capturing nearly all of the flow (Fig. 2 *A, C, D*, see *Supporting Information* for details). In contrast, under the high flow treatment, the flow-induced detachment is increased so that both genotypes form much thinner biofilms (Fig. 2 *E*), and this allows both to maintain access to flow for the entire duration of the experiment (Fig. 2 *B, C*). Each treatment was repeated three times, and each yielded the same results at steady-state (Fig. S3). Access to flow is essential for biofilms to acquire nutrients and disperse progeny downstream: these results suggest that the strength of the ambient flow places a key limitation on how rapidly a biofilm can expand without diverting its flow supply to genotypes that form thinner biofilms.

A mathematical model of flow-biofilm interaction reveals a diversity of competitive regimes and enables prediction of how cell dispersal varies in experiments. Our microfluidic competition experiments suggest that hydrodynamic interactions between biofilms can profoundly affect genotypic competition. In order to understand this process better, we next developed a model that couple two competing biofilms with a model of flow, enabling us to explore a much wider range of competitive scenarios. While the two pores in our experiment are strongly coupled, such that flow diverted from one pore is fully absorbed by the other pore, in a network of pores the strength of the hydrodynamic coupling between two competing biofilms will vary depending on the geometry of the pore space and their relative proximity to one another (Fig. 1 *A, B, C*). To account for this, we consider two identical fluid pathways of width $2L$ colonized by biofilms of thickness k_1 and k_2, which are connected in parallel to a channel of width $2M$ that does not contain biofilm (Fig. 1 *E*). The dimensionless parameter $M^* = M/L$ then measures the ability for the two biofilms to influence one another via flow: $M^* = 0$ corresponds to the strong coupling observed in our experiments (which lack a third channel without biofilm), whereas for increasing M^* flow is more likely to be diverted around the focal biofilms as they proliferate. Importantly, for $M^* > 0$, both biofilms are capable of clogging. This model then provides us a tractable way to resolve how changing the strength of the hydrodynamic in-

teraction between two biofilms affects their dynamics, without requiring an explicit representation of the pore structure.

A wide range of physical and biological processes can affect biofilm development [43], however, the thickness of biofilms in flowing environments is chiefly governed by the balance between cell division and flow induced detachment [44, 45]. Cell division in biofilms is often confined to a layer at the exterior of the biofilm, where substrates are exposed to nutrients from the flow [46, 47]. The characteristic thickness, δ, of this metabolically active layer is set by the balance of the diffusion of the substrate into the biofilm with its consumption, which yields the expression $\delta = \sqrt{2c_0DY/\alpha}$ [48], where c_0 is the substrate's concentration at the outer surface of the biofilm, D is the diffusion coefficient of the substrate in the biofilm, α is the bacterial growth rate, and Y the yield with which cells convert substrate to biomass. The rate at which the biofilm increases in thickness due to cell division is then given by the product of the growth rate, α, and $\min(\delta, k)$, such that $dk/dt = \alpha \min(\delta, k)$, which takes into account that the entire thickness of a biofilm is actively growing when $k < \delta$. Increases in biofilm thickness are countered by the detachment of cells due to mechanical forces exerted at the surface of the biofilm by fluid motion [40]. While the literature contains a diversity of parameterizations to model flow-induced biofilm detachment (see [49] for a comprehensive review), a formulation based on the empirical study of [50] is one of the most widely used [45, 51, 52, 53, 54, 55] and has been independently confirmed for biofilms growing in porous media [54, 55]. Here the detachment rate is approximated by $dk/dt = -\chi k\tau^{1/2}$, where χ is an empirical parameter with units of $\sqrt{\text{length/mass}}$ that measures the ability of the biofilm to resist detachment, and τ is the shear stress exerted by the flow on the surface of the biofilm. As such, we model changes in the thickness of biofilm via the superposition of cell division growth and flow-induced detachment,

$$\frac{dk_i}{dt} = \alpha_i \min(\delta_i, k_i) - \chi k_i \tau^{1/2}, \qquad [1]$$

where $\delta_i = \sqrt{2c_0DY/\alpha_i}$.

We used our model to simulate the development of two biofilms, which grow at rates α_1 and α_2, respectively and are coupled using our simplified flow model (Fig. 1 *E, F, Materials and Methods*). In the first instance we assume that both biofilms can equally resist detachment, but later this assumption is relaxed (see below). To reduce the number of tunable parameters, we non-dimensionalized the coupled differential equations governing the biofilm thicknesses, k_i, to yield four dimensionless parameters: $\alpha^* = \alpha_2/\alpha_1$, the ratio of growth rate of the two biofilms, $\beta^* = \sqrt{3\mu Q_T\chi^2/4BL^2\alpha_1^2}$, the strength of flow induced detachment normalized by the growth rate of the slower growing biofilm, $\delta^* = \sqrt{2c_0DY/\alpha_1L^2}$ the non-dimensional growing edge thickness of the slower growing biofilm, and $M^* = M/L$ the strength of the hydrodynamic coupling between the two biofilms. We initialized each pore with a thin biofilm layer ($k_i/L = 0.01$), which assumes that both strains can initially adhere surfaces equally well, and then we calculated the thicknesses of the two biofilms until they reached steady state. To isolate how the relative strength of the flow affected the biofilms, we fixed $\delta^* = 0.3$ and $M^* = 1$ to focus our attention on the $[\alpha^*, \beta^*]$ phase plane.

Our model predicted a diversity of different ecological outcomes (Figs. 3, S4). When flow was relatively weak ($\beta^* < 0.8$), biofilm growth dominated detachment, such that the positive feedback between increased flow diversion and reduced detachment ultimately led to both biofilms fully blocking their pore spaces (region c). In the opposite limit when flow was relatively strong ($\beta^* \geq 1.5$), detachment dominated the growth of the slower growing biofilm, which was completely scoured away from the surface. In this case, the faster growing genotype either fully detached (region a), reached a steady equilibrium thickness (region d), or blocked its own pore entirely (region e) depending on the asymmetry in growth rates, α^*. When the flow was at an intermediate level ($\beta^* \approx 0.8$ to 1.5), two outcomes were possible depending upon the value of α^*: if genotypes grew at a similar rate ($\alpha^* \approx 1$) the fast growing biofilm initially diverted flow away from its own pore space. However, as the thickness of slower growing biofilm increased over time, it diverted flow back towards the faster strain, and this stabilizing effect allowed both strains to access flow and disperse cells downstream at steady state, with the faster growing biofilm dispersing at a larger rate (Figs. 3 *b*, S4). If the asymmetry in the growth rates of the two strains was larger ($\alpha^* > 1$) in this intermediate flow regime, the slower growing strain was not able to stabilize the runaway growth of its neighbor and the faster growing genotype blocked its pore space (Fig. 3 *f*). Using the biofilm's dispersal rate at steady state, W, (equivalent to the rate at which new biofilm is formed at steady state) as an objective measure of fitness, our model indicates that slower growing biofilms are favored when flow is relatively weak, whilst faster growing biofilms are favored when flow is relatively strong. We note that our model assumes that cell dispersal is caused purely by flow-induced detachment and that bacteria do not actively regulate their propensity to detach.

The results from the model are in broad agreement with the two distinct flow regimes observed in our microfluidic experiments, which show that the wild-type biofilm growth tends to reduce its access to flow at smaller flow rates (equivalent to smaller β^*, Fig. 3 *f*), but is able to maintain access to flow at larger flow rates (equivalent to larger β^*, Fig. 3 *b*). While we could not directly measure rates of cell dispersal in our experiments, we combined our experimental data with a mechanistic model to predict how dispersal rate of each genotype changes over the course of our microfluidic experiments. First, we developed a model to translate the position of the dye interface h_D into the volumetric flow rates, q_i that pass through either arm of the device. This information was then combined with measurements of the biofilm thicknesses, k_i, to estimate the shear stress, τ_i, acting on the surface of either biofilm. Finally, both τ_i and k_i were used as inputs in the model of flow-induced biofilm detachment used above (see *Supporting Information* for details). This analysis shows that in the high flow rate treatment ($Q_T = 2$ ml h^{-1}), both biofilms gradually increase their dispersal rate until beginning to plateau after approximately 40 h (Fig. S6). In contrast, in the low flow treatment ($Q_T = 0.1$ ml h^{-1}) the wild-type biofilm rapidly increases its dispersal rate until it begins to divert its flow supply, which then causes a precipitous decrease in dispersal (Fig. S6). While the dye interface cannot be measured once the $\Delta rpoS$ flow path has captured $\approx 95\%$ of the flow (owing to the diffusion of the dye, see *Supporting Information*), by this point our analysis predicts that dispersal rate of the wild type biofilm has already dropped nearly three-fold from its peak value. During the same time period the $\Delta rpoS$ biofilm is predicted to sharply increase its rate of dispersal as it takes on the extra flow from the wild-type biofilm. While we cannot predict how the two genotypes differ in their rate of dispersal (*Supporting Information*), this analysis indicates that flow diversion can dramatically affect a biofilm's capacity to shed cells downstream.

The impact of flow on the evolution of bacterial growth rate. Our model shows that a biofilm's fate depends not only on

its growth rate, but also on the behavior of other biofilms elsewhere within the porous network. But how do hydrodynamic interactions between genotypes impact bacterial evolution? Over evolutionary timescales, it is expected that biofilm patches will repeatedly form and dissipate as a result of both natural processes and human intervention (e.g. predation [56, 57], enzymatic decay [58], and the periodic flushing of a porous filtration systems [59]). This continual turnover of biofilm patches means that if new genotypes are introduced into a network of pore spaces – whether through in-situ mutation or immigration – they will be able to form new patches and potentially compete with the resident genotype over many iterated rounds of competition. Our model can then be used a tool to measure the competitive ability of a newly introduced genotype, allowing us to infer how its frequency will change in the population over time.

To resolve how the bacterial growth rate would evolve over many successive rounds of competition, we embedded our mechanistic model of flow-biofilm interaction within a game theoretical framework known as adaptive dynamics [60]. Specifically, this invasion analysis tests whether a novel genotype that grows at rate α_M will be able to increase in frequency and ultimately supplant a population of biofilms that grow at rate α_R based on their relative fitness (*Materials and Methods*). Since the ability of a biofilm to seed new patches is expected to increase with its rate of dispersal, we again use this as a metric to quantify evolutionary fitness. A matrix of different α_R and α_M values is used to construct a so called pairwise invasibility plot (Fig. 4, [60]), which systematically delineates the growth rates for which a novel mutant can invade and displace the resident population. This representation then allows a generalized way to infer the trajectory of a population's growth rate over evolutionary timescales [60].

We find that mutants can invade only when their growth rate is slightly larger than the resident population (Fig. 4 *A*). However, over time successive invasions (Fig. 4 *A*, arrows) of new genotypes are predicted to systematically ratchet the up the growth rate of the resident population until it reaches a evolutionary stable value, α_{ESS}, after which no new genotypes will be able to invade (Fig. 4 *A*). Intuitively, when a biofilm that grows at α_{ESS} competes against a faster growing strain, the latter will block its pore space. Conversely, when a biofilm that grows at α_{ESS} competes against a slower growing strain the latter will disperse fewer cells downstream at steady state. We resolve how α_{ESS} varies as a function of the environmental conditions (Fig. 4 *B-D*). Increasing β^* – for example by increasing the total flow rate – leads to a larger α_{ESS}, whilst increasing the non-dimensional growing edge thickness δ^* – as can occur when nutrients are more plentiful – leads to a smaller α_{ESS}. Moreover, the connectivity of the porous structure also influences this process: increasing M^*, which increases the ability of flow to bypass the focal biofilms, leads to a reduction in α_{ESS}. All of these trends are consistent with the idea that increasing the potential for blocking, whether through lower flow rates, increased growing layer thickness, or an increased ability for flow to divert around competing biofilms, would promote the evolution of slower-growing genotypes. These results suggest that pore blocking places a fundamental physical limitation on the evolution of bacterial growth rates in porous environments, and stand in stark contrast with that observed in typical laboratory assays, such as within liquid batch cultures or chemostats, where evolution selects for the fastest growing genotype [16, 61].

Accounting for potential covariance between rates of bacterial growth and flow-induced detachment does not qualitatively affect our predictions. Our analyses above assume that a biofilm's growth rate can vary independently from its other phenotypic characteristics. However, previous experiments have shown that faster growing biofilms are more susceptible to flow induced detachment [62, 63, 64, 65]. This dependency may occur because fast growing genotypes invest less in secretions of exopolymeric substances that glue cells together [63] or because rapidly growing genotypes form biofilms with more fragile morphologies, rendering them more susceptible to detachment [66, 55]. To model how covariance between growth and detachment influences bacterial competition, we extended our model using the parameterization of Speitel and DiGiano [62], who empirically quantified this coupling in porous environments using radiolabelled carbon sources. This parameterization measures the strength of the coupling between growth and detachment with the non-dimensional parameter Φ^* (see *Supporting Information*, and [55, 62]): while our initial simulations (Fig. 3) assume $\Phi^* = 0$, a larger Φ^* indicates a stronger coupling between these two processes. Intuitively, a larger Φ^* reduces the potential that a genotype will block its pore space. While the inclusion of this new dependency changes the locations of the various competitive regimes in the $[\alpha^*, \beta^*]$ phase plane, their positions with respect to one another qualitatively remain the same (Fig. S5, *Supporting Information*). Thus, the conclusions from our original model ($\Phi^* = 0$), namely than faster growing genotypes are favored when flow is rapid, but are selected against when flow is weak, are robust to this additional dependency. Moreover, the inclusion of this additional term in our game-theoretical model reveals that a smaller Φ^* leads to a reduction in the predicted α_{ESS}, which is again consistent with the idea that increasing the potential for blocking reduces the evolutionary stable growth rate (Fig. 4 *E*). While it is possible that other phenotypic interdependencies could qualitatively affect microbial competition and evolution, these results indicate that the conclusions of our initial model still hold when a dependency between growth and detachment is included.

Discussion

Biofilms growing in porous environments facilitate a wide range of important processes in the natural environment and industry [67, 68, 69, 70, 26, 24, 25, 71, 72]. Our proof-of-principal experiments, mathematical modeling and game-theoretic analyses show that the feedback between biofilm proliferation and porous media hydrodynamics can dramatically affect how different genotypes compete. We find that relatively strong and weak flow conditions favor fast and slow growing biofilms respectively, while intermediate flow rates allow biofilms with different growth rates to maintain access to flow (Fig. 3).

In industrial settings, these new principles could be exploited to engineer microbial systems to favor a bacterial species with a particular growth rate, or keep multiple species with different growth rates active over longer time scales. For example, in porous wastewater reactors relatively fast growing species of bacteria convert ammonia to nitrite, but it is desirable to inhibit often slower growing species that further oxidize these products into nitrate, a potent environmental contaminant [73]. Our work predicts then that using a larger flow rate may be a way to favor the former species of bacteria over the latter. In contrast, the remediation of mercury contaminated wastewater in porous reactors can be enhanced by maintaining multiple species of bacteria that grow at different rates [74]. Moreover, our findings suggest that inoculating porous substrates with a community of cells from the effluent of a porous system would favor the growth of biofilms that do not block

their pore space, whilst inoculating cells from communities that have evolved in homogeneous laboratory conditions would promote blocking. Such information has implications for the design of effective water treatment systems, where blocking reduces efficiency, or in the design of bio-barriers to stifle the movement of groundwater contaminants, where blocking is the main objective.

Our results may also shed light on how cells compete in natural environments. We expect that heterogeneity in pore size and temporal fluctuations in flow will promote diversity. These are expected to be common due to geological processes that generate localized patches of different sized particles [75] and episodic patterns of rainfall. However, some groundwater aquifers and packed bed bioreactors have a more uniform distribution of pore spaces and nearly constant rates of flow, which may promote competitive exclusion. In systems where blocking does occur, natural selection may favor cells periodically detaching en masse to regain access to flow. Broadly consistent with this, increased detachment has been observed empirically in response to nutrient deprivation and quorum sensing [76, 77].

Bacteria are the subject of intense empirical and theoretical study. However, the vast majority of work on bacteria focuses on their behavior in liquid cultures or in simple biofilm assays. Here we have combined diverse bodies of theory, including fluid dynamics and game theory, to understand how bacteria compete and evolve within the complex porous environments where most bacteria live. Our assumptions greatly simplify the complexity of these systems, so there is considerable potential for useful extensions to our work. Many microbial traits can influence biofilm formation, including the strength of initial cell adhesion, which may itself be a function of the hydrodynamic or nutrient conditions [78, 21], production of extracellular polysaccharides [79], streamer formation [80, 30], quorum sensing [81], motility [82], and cell metabolism [83, 84]. Further work will be needed to resolve how the wide diversity of microbial traits impact the processes described here. Future efforts will also be required to resolve how the specific structure of the pore space and the distribution of different genotypes within them affect microbial competition. Nevertheless, our approaches indicate that porous habitats, and the flows within them, can have a profound impact on bacterial evolution. While rapid division gives a microbe a distinct advantage in typical laboratory environments, our results suggest that this paradigm does not extend to the majority of bacterial habitats.

Materials and Methods

Modelling Stokes flow through a representative network of pore spaces.

The geometry of the pore space (Fig. 1A-C) was obtained using PFC2D (Particle Flow Code in Two Dimensions, ITSCA), which models the mechanical processes that form many porous substrates. The particle locations were then imported into COMSOL Multiphysics to model incompressible Stokes flow within the pore spaces between the particles using the finite element method. Zero flux, no slip boundary conditions were used at the left and right boundaries of the computational domain as well as on the surfaces of all the particles. At the top and bottom boundaries of the computational domain the pressure was fixed at two different values, such that the resulting pressure gradient was responsible for driving flow. The Stokes equations were solved with and without the presence of a biofilm "patch" in one of the pore spaces. Results were then exported into Matlab 2015a (MathWorks) for further analysis and plotting.

Bacterial strains and culturing.

Our experiments used *Escherichia coli* strain K12-W3110 and a mutant with a rpoS819 allele insertion [85, 86]. Each strain was labeled with either green fluorescent protein (GFP) or red fluorescent protein (RFP). Cell cultures were grown overnight in Tryptone broth (1 x TB, 10 g Bactotryptone per 1 L water) at 37°C, diluted to an optical density of 0.1 (at 600 nm), and then grown for a further hour at 37°C so that cells were in exponential phase when they were first introduced into the microfluidic devices.

Competition Experiments.

Microfluidic device masters were fabricated from SU-8 on silicon wafers using standard soft lithography techniques [87] and were cast with polydimethylsiloxane (PDMS, Sylgard 184, Dow Corning). The depth of these devices was $2B$= 75 μm (Fig. S1). Cured PDMS was bonded to glass coverslips (50 mm by 75 mm, No. 1 thickness, Agar Scientific) with a corona discharge system (BD-20AC, Electro-Technic Products) using previously described techniques [88]. Tygon tubing (Microbore, 0.51 mm inner radius) was used to plumb the inlets and outlets of the device.

For the high-flow rate treatments (Q_T=2 ml h^{-1}) the outlet was connected to a 140 mL syringe (Harvard Apparatus), which was mounted on a Harvard Apparatus 2000 syringe pump. In the low-flow treatments (Q_T=0.1 ml h^{-1}), the outlet was connected to a 20 mL syringe (Becton Dickinson) mounted on a Harvard Apparatus PhD Ultra syringe pump.

After the microfluidic device and tubing was primed with 1 x TB to remove air from the system, cells were introduced into the device by pulling cultures of the wild type and $\Delta rpoS$ mutant cells through the device at Q_T=0.1 ml h^{-1}. Unlike many biofilm experiments, where cells are allowed to attach to surfaces in the absence of flow (e.g. [89, 17, 90]), we inoculated cells under flow to help keep the two strains confined to their respective pore spaces. Cultures of the wild type and $\Delta rpoS$ mutant were simultaneously drawn through the device for 20 hours to allow cells to attach and then we switched over to withdrawing tryptone broth (0.5 x TB, 5 g Tryptone per liter of water) through the device for a further 48 hours so that a thin biofilm was established in each of the pore spaces. We initiated the biofilms in the high and low flow treatments in the same way in the first three days of the experiment to ensure that the cell attachment was similar between the two treatments. After this initial inoculation phase, we connected one of the inlets of the device to a reservoir containing tryptone broth (0.5 x TB) mixed with dye (Chicago Blue, Sigma Aldrich) that enabled us to dynamically track the relative proportion of flow passing through each side of the device.

After the initial inoculation phase, we applied a flow rate of Q_T=2 ml h^{-1} in the high flow rate treatment, whereas in the low flow rate treatment we used a flow rate of Q_T=0.1 ml h^{-1}. We imaged the devices every thirty minutes for the next 70 hours, which allowed both treatments to reach a steady state. Each treatment was repeated 3 times and each of these yielded the same result at steady state (Fig. S3). The time points shown in Fig. 2 and Fig. S3 are measured from the end of the inoculation phase.

Mechanistic model of biofilm competition.

Our mathematical model of biofilm competition simulates the two processes that are predicted to dominate biofilm development in flowing environments: bacterial growth and the flow induced detachment [45, 52]. The differential equations that govern the thicknesses of the two biofilms, k_i (Eqn. 1, main text) are hydrodynamically coupled using an approach that is widely used for low Reynolds number flows [91]. Specifically, we consider three flow paths of equal length connected in parallel, so the total volumetric flow rate, Q_T, divides among the three pathways as a function of their hydrodynamic resistances, R_i. Poiseulle's law states that $q_i = -dP/R_i$, where q_i is the flow rate along each path, dP is the drop in pressure across the system, and $R_i = 3\mu/4B(L-k_i)^3$ is the hydrodynamic resistance per unit length of each flow path, where μ is the dynamic velocity of the fluid, $2B$ is the span wise dimension of the pore space, $2L$ is the pore width as described in the main text, and $L \ll B$.

All three flow paths experience the same difference in pressure, $dP = -Q_T R_T$, which is determined by the effective resistance of the entire system, R_T, where [91]:

$$\frac{1}{R_T} = \frac{1}{R_1} + \frac{1}{R_2} + \frac{1}{R_3}. \qquad [2]$$

Solving for dP and substituting into the equation for q_i yields:

$$q_i = \frac{Q_T}{R_i} \frac{1}{1/R_1 + 1/R_2 + 1/R_3}, \qquad [3]$$

which, can then be written in terms of the biofilm thicknesses,

$$q_i = Q_T \frac{(L-k_i)^3}{(L-k_1)^3+(L-k_2)^3+M^3}. \quad [4]$$

This expression conserves flow, so that $Q_T = q_1 + q_2 + q_3$. We note that the approach used here is analogous to that routinely used in the analysis of electric circuits [91].

Our equation for hydrodynamic resistance assumes pressure driven, planar flow between two parallel plates separated by a distance $2(L-k_i)$, where the velocity profile in the ith channel is given by $u(y)=-\frac{dP}{2\mu}(y^2-(L-k_i)^2)$ and y is the distance from the centerline of the channel. Thus, the hydrodynamic shear stress acting on the biofilm is given by

$$\tau = \mu\frac{du}{dy} = \frac{3\mu q_i}{4B(L-k_i)^2}, \quad [5]$$

where du/dy has been evaluated at the biofilm's surface, $y = L - k_i$.

Combining Eqns. (1), (4) and (5) yields the coupled differential equations that govern k_1 and k_2, the thicknesses of the two biofilms:

$$\frac{dk_1}{dt} = \alpha_1 \min(\delta_1, k_1) - k_1\sqrt{\frac{3\mu Q_T \chi^2}{4B}}\sqrt{\frac{(L-k_1)}{(L-k_1)^3+(L-k_2)^3+M^3}}, \quad [6]$$

$$\frac{dk_2}{dt} = \alpha_2 \min(\delta_2, k_2) - k_2\sqrt{\frac{3\mu Q_T \chi^2}{4B}}\sqrt{\frac{(L-k_2)}{(L-k_1)^3+(L-k_2)^3+M^3}}. \quad [7]$$

We non-dimensionalized the governing equations above using the pore half-width L as our characteristic length scale and the reciprocal growth rate of strain 1, $1/\alpha_1$, as our characteristic time scale, such that $k_1{=}Lk_1^*, k_2{=}Lk_2^*, M{=}LM^*$, and $t{=}t^*/\alpha_1$. This yields the dimensionless equations

$$\frac{dk_1}{dt} = \min(k_1, \delta^*) - \beta^* k_1\sqrt{\frac{(1-k_1)}{\theta}}, \quad [8]$$

$$\frac{dk_2}{dt} = \alpha^* \min(k_2, \frac{\delta^*}{\sqrt{\alpha^*}}) - \beta^* k_2\sqrt{\frac{(1-k_2)}{\theta}}, \quad [9]$$

$$\text{where } \theta = (1-k_1)^3 + (1-k_2)^3 + (M^*)^3, \quad [10]$$

where we have omitted the stars from k_i and t for clarity. These equations were solved numerically using Matlab. Specifically, we initialized two pore spaces with a thin layer of biofilm, $k_1 = k_2 = 0.01$, similar to the initially sparse seeding of cells in our experiments (see Fig. 2 and previous section). We then solved these equations until each biofilm had converged to a steady state thickness. We repeated this process for different combinations of the non-dimensional parameters $\alpha^*, \beta^*, \delta^*$, and M^*, in order to build the parameter spaces in Fig. 3 and 4.

Game theoretical analysis.

To examine how hydrodynamic interactions impact biofilm evolution we embedded the mechanistic model presented above within an adaptive dynamics framework [92, 60]. This examines whether a new genotype is able to invade and displace a porous environment already colonized by "resident" genotype. Specifically, this assumes that the rate at which novel genotypes are introduced into a group of interacting pore spaces – either through in-situ mutation or immigration – is small compared to the rate at which a new genotype can displace the resident population [93]. This assumption means that we can consider the pairwise interaction of a novel genotype that grows at α_M with a monomorphic resident population growing at α_R.

We assumed that the fitness of a genotype is directly proportional to its rate of cell dispersal at steady state, which is equal to the rate of biofilm growth at steady state (Eqn. 1). Specifically, the fitness of a biofilm, W, is a function of its growth rate, its competitor's growth rate, and the properties of the pore space (Fig. 3). Two conditions must then hold for a "mutant" to supplant the resident genotype. First, the fitness of the mutant when competing against the resident, denoted $W(\alpha_M, \alpha_R)$, must be larger than or equal to that of the resident competing against itself, $W(\alpha_R, \alpha_R)$. This determines whether an initially rare mutant is able to gradually increase in frequency within the population. Second, the fitness of the resident when competing against the mutant, $W(\alpha_R, \alpha_M)$, must be smaller than that of the mutant competing against itself $W(\alpha_M, \alpha_M)$. This determines if the original resident growth strategy will be able to re-invade the system once the mutant has increased in frequency. More formally, the following two criteria must hold for a mutant to invade a resident population:

$$W(\alpha_M, \alpha_R) \geq W(\alpha_R, \alpha_R), \quad [11]$$

$$W(\alpha_R, \alpha_M) < W(\alpha_M, \alpha_M). \quad [12]$$

These criteria are then used to construct a pairwise invasibility plot (Fig. 4, [60]), which can be used to infer the evolutionary trajectory of the population's growth rate.

ACKNOWLEDGMENTS.

We thank Juan Keymer for bacterial strains. K.Z.C. was funded by the Engineering and Physical Sciences Research Council, K.R.F. by the European Research Council (242670) and W.M.D by the Human Frontier Science Program (LT001181/2011L).

1. Azam F, Malfatti F (2007) Microbial structuring of marine ecosystems. Nature reviews. Microbiology 5(10):782–91.
2. Schluter J, Foster KR (2012) The evolution of mutualism in gut microbiota via host epithelial selection. PLoS biology 10(11):e1001424.
3. Bever JD, Richardson SC, Lawrence BM, Holmes J, Watson M (2009) Preferential allocation to beneficial symbiont with spatial structure maintains mycorrhizal mutualism. Ecology letters 12(1):13–21.
4. Horner-Devine MC, Carney KM, Bohannan BJM (2004) An ecological perspective on bacterial biodiversity. Proceedings of the Royal Society B: Biological Sciences 271(1535):113–22.
5. Franzosa EA et al. (2015) Sequencing and beyond: integrating molecular 'omics' for microbial community profiling. Nature Reviews Microbiology 13(6):360–372.
6. Allen EE, Banfield JF (2005) Community genomics in microbial ecology and evolution. Nature reviews microbiology 3(6):489–98.
7. Rusconi R, Garren M, Stocker R (2014) Microfluidics Expanding the Frontiers of Microbial Ecology. Annual Review of Biophysics 43(1):65–91.
8. Whitman WB, Coleman DC, Wiebe WJ (1998) Perspective Prokaryotes : The unseen majority. Proceedings of the National Academy of Sciences of the United States of America 95(June):6578–6583.
9. Ghiorse WC, Wilson JT (1988) Advances in Applied Microbiology, Advances in Applied Microbiology. (Elsevier) Vol. 33, pp. 107–172.
10. Torsvik V (2002) Prokaryotic Diversity–Magnitude, Dynamics, and Controlling Factors. Science 296(5570):1064–1066.
11. Rothman DH, Forney DC (2007) Physical model for the decay and preservation of marine organic carbon. Science (New York, N.Y.) 316(5829):1325–8.
12. Moons P, Michiels CW, Aertsen A (2009) Bacterial interactions in biofilms. Critical Reviews in Microbiology 35:157–168.
13. Xavier JB, Foster KR (2007) Cooperation and conflict in microbial biofilms. Proceedings of the National Academy of Sciences of the United States of America 104(3):876–81.
14. Nadell CD, Xavier JB, Levin SA, Foster KR (2008) The evolution of quorum sensing in bacterial biofilms. PLoS Biology 6(1):0171–0179.
15. Rao D, Webb JS, Kjelleberg S (2005) Competitive interactions in mixed-species biofilms containing the marine bacterium Pseudoalteromonas tunicata. Applied and environmental microbiology 71(4):1729–36.
16. Hibbing ME, Fuqua C, Parsek MR, Peterson SB (2010) Bacterial competition: surviving and thriving in the microbial jungle. Nature reviews microbiology 8(1):15–25.
17. Klausen M et al. (2003) Biofilm formation by Pseudomonas aeruginosa wild type, flagella and type IV pili mutants. Molecular Microbiology 48(6):1511–1524.
18. Kim W, Racimo F, Schluter J, Levy SB, Foster KR (2014) Importance of positioning for microbial evolution. Proceedings of the National Academy of Sciences of the United States of America 111(16):E1639–47.
19. Stoodley P et al. (2001) Growth and detachment of cell clusters from mature mixed-species biofilms. Applied and environmental microbiology 67(12):5608–13.
20. Chambless JD, Stewart PS (2007) A three-dimensional computer model analysis of three hypothetical biofilm detachment mechanisms. Biotechnology and bioengineering 97(6):1573–84.
21. Zhang W, Sileika T, Packman AI (2013) Effects of fluid flow conditions on interactions between species in biofilms. FEMS microbiology ecology 84(2):344–354.
22. Thullner M (2010) Comparison of bioclogging effects in saturated porous media within one- and two-dimensional flow systems. Ecological Engineering 36(2):176–196.
23. Cunningham AB, Sharp RR, Hiebert R, James G (2003) Subsurface Biofilm Barriers for the Containment and Remediation of Contaminated Groundwater. Bioremediation Journal 7(3-4):151–164.
24. Wang X, Hendry P (2012) Effect of Nutrient Addition on an Oil Reservoir Microbial Population: Implications for Enhanced Oil Recovery. Journal of Petroleum & Environmental Biotechnology 03.
25. Nicolella C, van Loosdrecht MC, Heijnen JJ (2000) Wastewater treatment with particulate biofilm reactors. Journal of biotechnology 80(1):1–33.
26. Kim JW, Choi H, Pachepsky Ya (2010) Biofilm morphology as related to the porous media clogging. Water Research 44(4):1193–201.

27. Cunningham A, Characklis W, Abedeen F, Crawford D (1991) Influence of biofilm accumulation on porous media hydrodynamics. Environment Science Technology pp. 1305–1311.
28. Shafahi M, Vafai K (2009) Biofilm affected characteristics of porous structures. International Journal of Heat and Mass Transfer 52(3-4):574–581.
29. von der Schulenburg DG, Pintelon T, Picioreanu C, Van Loosdrecht M, Johns M (2009) Three-dimensional simulations of biofilm growth in porous media. AIChE journal pp. 494–504.
30. Drescher K, Shen Y, Bassler BL, Stone HA (2013) Biofilm streamers cause catastrophic disruption of flow with consequences for environmental and medical systems. Proceedings of the National Academy of Sciences of the United States of America 110(11):4345–50.
31. Dupin HJ, Kitanidis PK, McCarty PL (2001) Pore-scale modeling of biological clogging due to aggregate expansion: A material mechanics approach. Water Resources Research 37(12):2965.
32. Nadell CD, Foster KR, Xavier JB (2010) Emergence of spatial structure in cell groups and the evolution of cooperation. PLoS computational biology 6(3):e1000716.
33. Millet YA et al. (2014) Insights into Vibrio cholerae intestinal colonization from monitoring fluorescently labeled bacteria. PLoS pathogens 10(10):e1004405.
34. Mitri S, Foster KR (2013) A Genotypic View of Social Interactions in Microbial Communities. Annual Review of Genetics 47:265–91.
35. Hallatschek O, Hersen P, Ramanathan S, Nelson DR (2007) Genetic drift at expanding frontiers promotes gene segregation. Proceedings of the National Academy of Sciences of the United States of America 104(50):19926–30.
36. van Gestel J, Weissing FJ, Kuipers OP, Kovács AT (2014) Density of founder cells affects spatial pattern formation and cooperation in Bacillus subtilis biofilms. The ISME journal 8(10):2069–79.
37. Pintelon TRR, Graf von der Schulenburg Da, Johns ML (2009) Towards optimum permeability reduction in porous media using biofilm growth simulations. Biotechnology and bioengineering 103(4):767–79.
38. Adams JL, McLean RJ (1999) Impact of rpoS deletion on Escherichia coli biofilms. Applied and environmental microbiology 65(9):4285–7.
39. Ito A, May T, Kawata K, Okabe S (2008) Significance of rpoS during maturation of Escherichia coli biofilms. Biotechnology and bioengineering 99(6):1462–71.
40. Trulear M, Characklis W (1982) Dynamics of biofilm processes. Water Pollution Control Federation 54(9):1288–1301.
41. Stoodley P, Cargo R, Rupp CJ, Wilson S, Klapper I (2002) Biofilm material properties as related to shear-induced deformation and detachment phenomena. Journal of industrial microbiology & biotechnology 29(6):361–7.
42. Stewart PS (1993) A model of biofilm detachment. Biotechnology and bioengineering 41(1):111–7.
43. Donlan RM (2002) Biofilms: microbial life on surfaces. Emerging infectious diseases 8(9):881–90.
44. Van Loosdrecht MCM et al. (1995) Biofilm structures. Water Science and Technology 32(8):35–43.
45. Duddu R, Chopp DL, Moran B (2009) A two-dimensional continuum model of biofilm growth incorporating fluid flow and shear stress based detachment. Biotechnology and bioengineering 103(1):92–104.
46. Williamson K, McCarty PL (1976) A model of substrate utilization by bacterial films. Journal - Water Pollution Control Federation 48(1):9–24.
47. Werner E et al. (2004) Stratified growth in Pseudomonas aeruginosa biofilms. Applied and environmental microbiology 70(10):6188–96.
48. Pirt S (1967) A kinetic study of the mode of growth of surface colonies of bacteria and fungi. Journal of General Microbiology pp. 181–197.
49. Horn H, Lackner S (2014) Modeling of biofilm systems: a review. Advances in biochemical engineering/biotechnology 146:53–76.
50. Rittmann B (1982) The effect of shear stress on biofilm loss rate. Biotechnology and Bioengineering 24(2).
51. Abbas F (2011) Mathematical Contributions to One-dimensional Biofilm Modeling, PhD Thesis. The University of Guelph.
52. Abbas F, Sudarsan R, Eberl HJ (2012) Longtime behavior of one-dimensional biofilm models with shear dependent detachment rates. Mathematical Biosciences and Engineering 9(2):215–239.
53. Wanner O, Gujer W (1986) A Multispecies Biofilm Model. Biotechnology and Bioengineering 28:314328.
54. Brovelli A, Malaguerra F, Barry DA (2009) Bioclogging in porous media: Model development and sensitivity to initial conditions. Environmental Modelling & Software 24(5):611–626.
55. Ebigbo A, Helmig R, Cunningham AB, Class H, Gerlach R (2010) Modelling biofilm growth in the presence of carbon dioxide and water flow in the subsurface. Advances in Water Resources 33(7):762–781.
56. Lawrence J, Scharf B, Packroff G, Neu T (2002) Microscale evaluation of the effects of grazing by invertebrates with contrasting feeding modes on river biofilm architecture and composition. Microbial Ecology 44(3):199–207.
57. DeLeo PC, Baveye P (1997) Factors affecting protozoan predation of bacteria clogging laboratory aquifer microcosms. Geomicrobiology Journal 14(2):127–149.
58. Allison DG, Ruiz B, SanJose C, Jaspe A, Gilbert P (1998) Extracellular products as mediators of the formation and detachment of pseudomonas fluorescens biofilms. FEMS microbiology letters 167(2):179–184.
59. Moreira M, Feijoo G, Palma C, Lema J, et al. (1997) Continuous production of manganese peroxidase by phanerochaete chrysosporium immobilized on polyurethane foam in a pulsed packed-bed bioreactor. Biotechnology and bioengineering 56(2):130–137.
60. Brännström Å, Johansson J, von Festenberg N (2013) The Hitchhiker's Guide to Adaptive Dynamics. Games 4(3):304–328.
61. Ibarra RU, Edwards JS, Palsson BO (2002) Escherichia coli k-12 undergoes adaptive evolution to achieve in silico predicted optimal growth. Nature 420(6912):186–189.
62. Speitel G, DiGiano F (1987) Biofilm shearing under dynamic conditions. Journal of Environmental Engineering 113(21534):464–475.
63. Robinson JA, Trulear MG, Characklis WG (1984) Cellular reporoduction and extracellular polymer formation by pseudomonas aeruginosa in continuous culture. Biotechnology and bioengineering 26(12):1409–1417.
64. Clement T, Hooker B, Skeen R (1996) Macroscopic models for predicting changes in saturated porous media properties caused by microbial growth. Ground Water 34(5):934–942.
65. Peyton BM, Characklis W (1993) A statistical analysis of the effect of substrate utilization and shear stress on the kinetics of biofilm detachment. Biotechnology and Bioengineering 41(7):728–735.
66. Picioreanu C, van Loosdrecht MC, Heijnen JJ (2001) Two-dimensional model of biofilm detachment caused by internal stress from liquid flow. Biotechnology and bioengineering 72(2):205–18.
67. Whitman WB, Coleman DC, Wiebe WJ (1998) Perspective Prokaryotes : The unseen majority. Proceedings of the National Academy of Sciences of the United States of America 95(12):6578–6583.
68. Danhorn T, Fuqua C (2007) Biofilm formation by plant-associated bacteria. Annual review of microbiology 61:401–422.
69. De Muynck W, De Belie N, Verstraete W (2010) Microbial carbonate precipitation in construction materials: A review. Ecological Engineering 36(2):118–136.
70. Mitchell AC, Dideriksen K, Spangler LH, Cunningham AB, Gerlach R (2010) Microbially enhanced carbon capture and storage by mineral-trapping and solubility-trapping. Environmental science & technology 44(13):5270–6.
71. Leite J, Fernandes B, Pozzi E (2008) Application of an anaerobic packed-bed bioreactor for the production of hydrogen and organic acids. International Journal of Hydrogen Energy 33(2):579–586.
72. Michalakos G, Nieva J, Vayenas D, Lyberatos G (1997) Removal of iron from potable water using a trickling filter. Water research 31(5):991–996.
73. Cho S, Fujii N, Lee T, Okabe S (2011) Development of a simultaneous partial nitrification and anaerobic ammonia oxidation process in a single reactor. Bioresource technology 102(2):652–9.
74. Von Canstein H, Kelly S, Li Y, Wagner-Döbler I (2002) Species diversity improves the efficiency of mercury-reducing biofilms under changing environmental conditions. Applied and environmental microbiology 68(6):2829–37.
75. Rehfeldt KR, Boggs JM, Gelhar LW (1992) Field study of dispersion in a heterogeneous aquifer: 3. Geostatistical analysis of hydraulic conductivity. Water Resources Research 28(12):3309–3324.
76. Kong KF, Vuong C, Otto M (2006) Staphylococcus quorum sensing in biofilm formation and infection. International Journal of Medical Microbiology 296(2-3):133–9.
77. Sauer K et al. (2004) Characterization of nutrient-induced dispersion in Pseudomonas aeruginosa PAO1 biofilm. Journal of bacteriology 186(21):7312–26.
78. Lecuyer S et al. (2011) Shear stress increases the residence time of adhesion of pseudomonas aeruginosa. Biophysical journal 100(2):341–350.
79. Danese PN, Pratt LA, Kolter R (2000) Exopolysaccharide production is required for development of escherichia coli k-12 biofilm architecture. Journal of bacteriology 182(12):3593–3596.
80. Valiei A, Kumar A, Mukherjee PP, Liu Y, Thundat T (2012) A web of streamers: biofilm formation in a porous microfluidic device. Lab on a chip 12(24):5133–7.
81. Hammer BK, Bassler BL (2003) Quorum sensing controls biofilm formation in vibrio cholerae. Molecular microbiology 50(1):101–104.
82. Zhao K et al. (2013) Psl trails guide exploration and microcolony formation in pseudomonas aeruginosa biofilms. Nature 497(7449):388–391.
83. Bjergbæk LA, Haagensen JAJ, Reisner A, Molin S, Roslev P (2007) Effect of oxygen and growth medium on in vitro biofilm formation by Escherichia coli. Biofilms 3(01):1–10.
84. Colón-González M, Méndez-Ortiz MM, Membrillo-Hernández J (2004) Anaerobic growth does not support biofilm formation in Escherichia coli K-12. Research in microbiology 155(7):514–21.
85. Keymer JE, Galajda P, Lambert G, Liao D, Austin RH (2008) Computation of mutual fitness by competing bacteria. Proceedings of the National Academy of Sciences of the United States of America 105(51):20269–73.
86. Lambert G, Liao D, Vyawahare S, Austin RH (2011) Anomalous spatial redistribution of competing bacteria under starvation conditions. Journal of Bacteriology 193(8):1878–83.
87. Whitesides G, Ostuni E, Takayama S, Jiang X, Ingber D (2001) Soft lithography in biology and biochemistry. Annu Rev Biomed Eng 3:335–73.
88. Haubert K, Drier T, Beebe D (2006) PDMS bonding by means of a portable, low-cost corona system. Lab on a chip 6(12):1548–9.
89. Moller S et al. (1998) In Situ Gene Expression in Mixed-Culture Biofilms: Evidence of Metabolic Interactions between Community Members. Appl. Envir. Microbiol. 64(2):721–732.
90. Drenkard E, Ausubel FM (2002) Pseudomonas biofilm formation and antibiotic resistance are linked to phenotypic variation. Nature 416(6882):740–3.
91. Stone HA (2007) Introduction to fluid dynamics for microfluidic flows, Series on Integrated Circuits and Systems eds. Lee H, Westervelt RM, Ham D. (Springer US, Boston, MA).
92. Diekmann ODO (2004) A beginner's guide to adaptive dynamics. 63:47–86.

93. Nowak MA, Sigmund K (2004) Evolutionary dynamics of biological games. Science 303(5659):793–799.
94. Schindelin J et al. (2012) Fiji: an open-source platform for biological-image analysis. Nature methods 9(7):676–82.
95. Sinton LW et al. (2010) Transport of Escherichia coli and F-RNA bacteriophages in a 5m column of saturated pea gravel. Journal of Contaminant Hydrology 117(1):71–81.
96. Biggar JW, Nielsen DR (1976) Spatial variability of the leaching characteristics of a field soil. Water Resources Research 12(1):78.
97. Dercole F, Rinaldi S (2008) Analysis of evolutionary processes: the adaptive dynamics approach and its applications. (Princeton University Press).
98. Valko E (1935) Measurements of the diffusion of dyestuffs. Transactions of the Faraday Society 31:230–245.

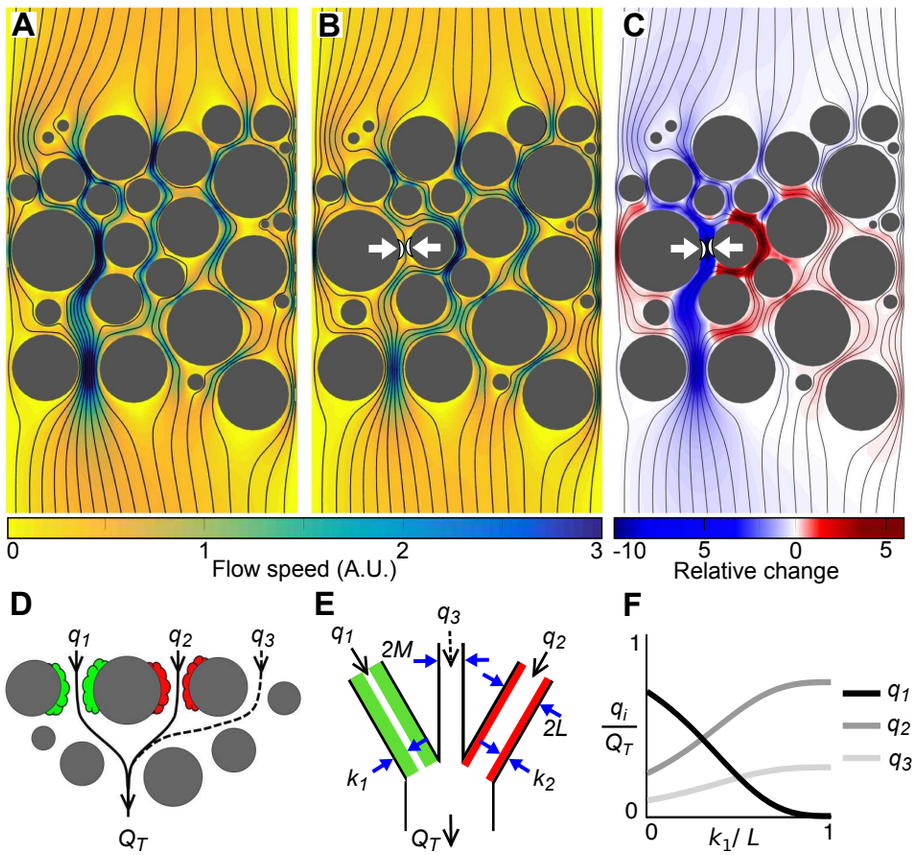

Fig. 1. A growing biofilm tends to decrease its access to flow whilst increasing the flow to its competitors. (A) Viscosity dominates inertia in most porous environments, owing to the relatively small pore spaces (10 μm - 1 mm) and slow fluid velocities (1 - 1000 $\mu m\ s^{-1}$) [95, 96], which allows flow to be modeled using the Stokes equations. Here, we numerically solved the Stokes equations within a representative two-dimensional porous geometry. Flow is driven by a fixed pressure difference between the top and bottom boundaries, whilst the left and right boundaries are impermeable (see $Materials\ and\ Methods$ for further details). Black lines show streamlines and the color map shows the flow speed in arbitrary units (A. U.). (B) The flow field after the addition of a small impermeable patch of biofilm (white arrows). All other parameters of the simulation remained constant. (C) The relative change in flow speed measured as $(s_a - s_b)/s_a$, where s_a is the initial flow speed and s_b is the flow speed after the addition of the biofilm patch, shows that the biofilm sharply decreases the flow through the pore in which it resides and increases the flow through neighboring pore spaces. (D) A cartoon of two biofilm patches (green, red) that interact hydrodynamically. The proportion of the total flow, Q_T, that moves past each biofilm changes as the biofilms grow and increase the hydrodynamic resistance of their respective pore spaces. A third flow path (dotted line) models the ability for flow to divert around the two competing biofilms. (E) Our conceptual model where two biofilms, with thicknesses k_1 and k_2, live along neighboring flow paths of width $2L$, that are connected to a flow path of width $2M$ that does not harbor any biofilm. The proportion of the total volumetric rate flow, Q_T, that passes along each of the three flow paths is calculated using Kirchoff's laws assuming planar Poiseuille flow in each pore space (see $Materials\ and\ Methods$). (F) Analogous to our Stokes flow simulations, if k_1 increases in thickness the proportion of the total flow rate through its pore space, q_1/Q_T, decreases, whilst increasing the amount of flow, q_2/Q_T, received by the neighboring biofilm. Here $k_2/L = 0.3$ and $M/L = 1$.

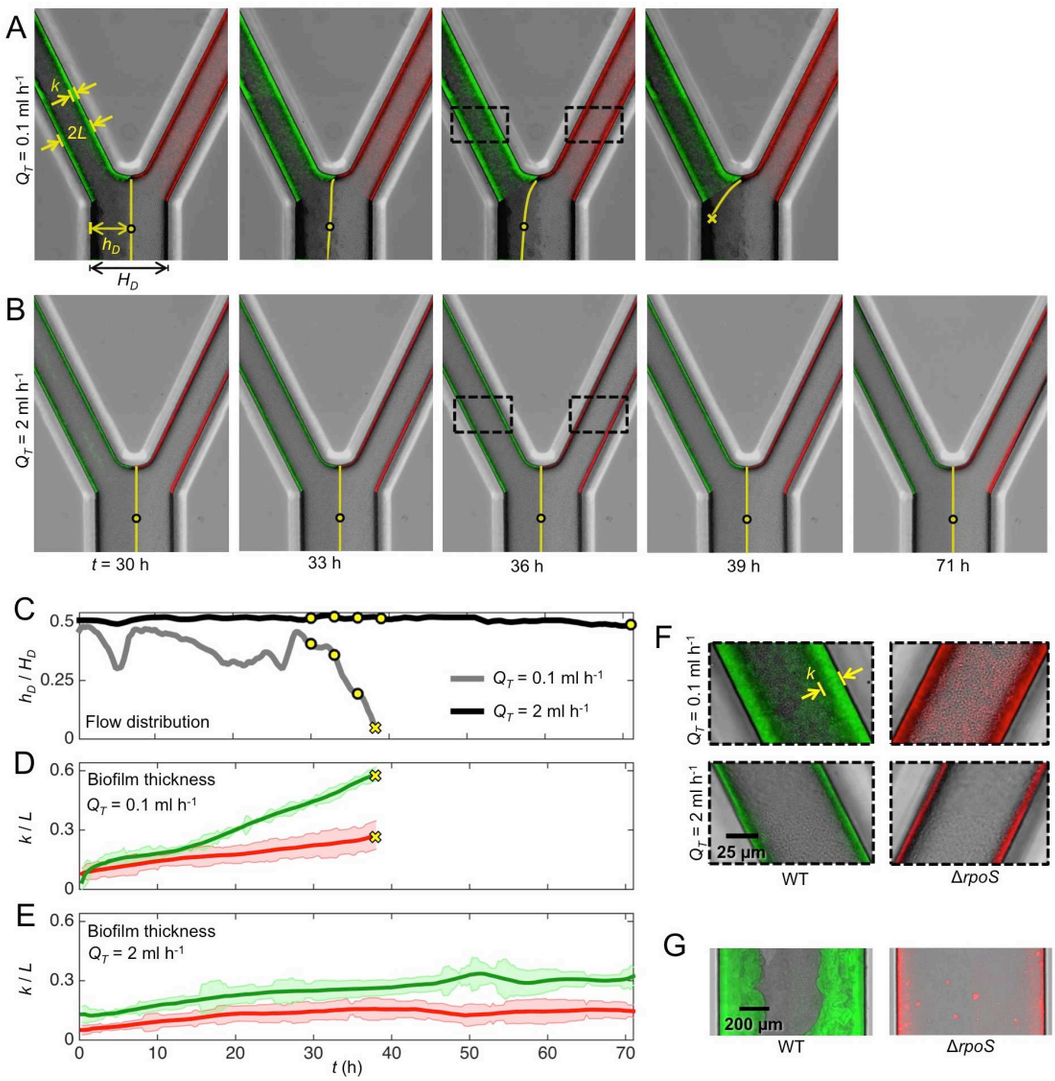

Fig. 2. Microfluidic competition experiments show that biofilms that rapidly increase in thickness tend to divert flow to biofilms that expand more more slowly. (A, B) The left pore of each device was seeded with wild-type cells (green), whereas the right pore was inoculated with $\Delta rpoS$ cells (red). Dyed media flows through the left pore, whereas clear media flows through the right pore. The dye interface downstream of the two pores (yellow line) allows us to dynamically track the proportion of the total flow, Q_T, moving through each pore space (*Materials and Methods*). (C) Following the movement of the dye interface (yellow circles in A, B) shows that in the weak flow treatment (A) the wild-type biofilm diverted nearly all its flow supply after 38 hours, such that subsequently the dye interface was not detectable at the measurement location (*Supporting Information*). However, in the strong flow treatment (B) both biofilms are able to maintain access to flow for more than 70 hours. (D, E) In the weak flow treatment the wild-type biofilm (green line) increased in thickness, k, faster than the $\Delta rpoS$ null biofilm (red line), which was responsible for the diversion of flow (see text). In strong flow, both biofilms were thinner, such that the difference in biofilm thickness between the two strains was smaller. Shaded regions show the standard deviation about the mean (*Materials and Methods*). (F) A magnified view of the biofilms shown within the dashed black rectangles in A and B. (G) The observation that wild type biofilms expand at a faster rate than $\Delta rpoS$ biofilms was confirmed in separate microfluidic experiments that exposed attached cells to much smaller shear stresses than in the competition experiment, which minimized the effect of flow induced detachment (*Supporting Information*). The upstream arms of the microfluidic devices used in the competition experiments (A-F) have a width of $2L = 65\ \mu m$ and depth of $2B = 75\ \mu m$ (Fig. S1).

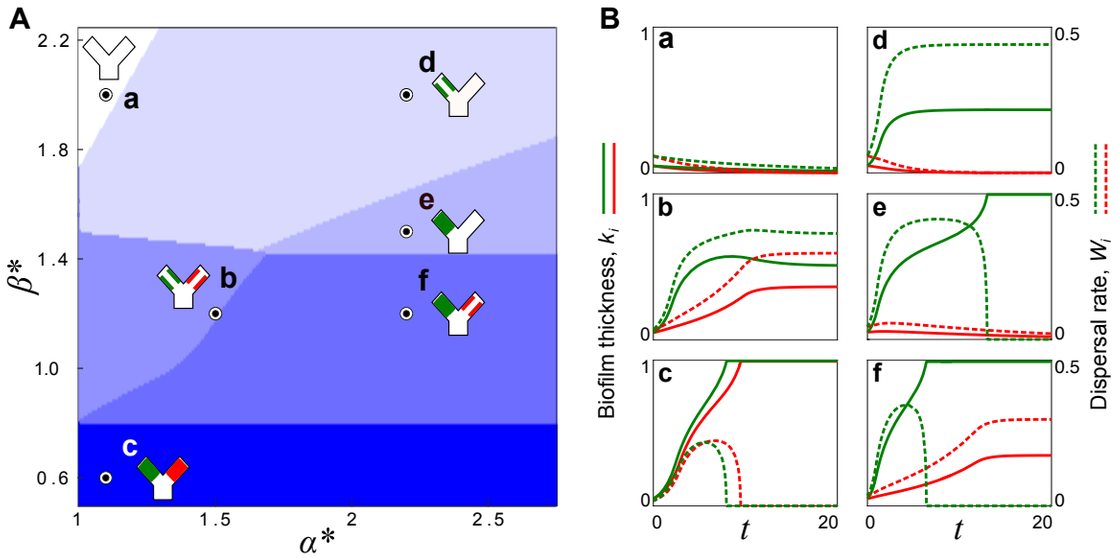

Fig. 3. Diverse ecological regimes emerge from a model of biofilm competition where two strains are coupled by flow. (A) The phase space formed by α^*, the growth rate of a fast growing biofilm (green) divided by that of a slower growing biofilm (red), and β^*, a non-dimensional parameter that measures the importance of flow induced biofilm detachment relative to that of biofilm growth, reveals six different regimes at steady-state. (B, a-f) Here we plot the biofilm thicknesses, k_1, k_2 (solid lines), and the dispersal rates, W_1, W_2 (dashed lines), for a representative simulation in each of the regimes (circles in A). When a biofilm is fully scoured from the surface ($k_i = 0$) or completely blocks its pore space ($k_i = 1$) its dispersal goes to zero ($W_i = 0$). In contrast, if a biofilm thickness reaches a non-trivial fixed point $0 < k_i < 1$, it disperses cells downstream at steady-state. Here $M^* = 1, \delta^* = 0.3$. For clarity, we have omitted the third flow path from the cartoons in A.

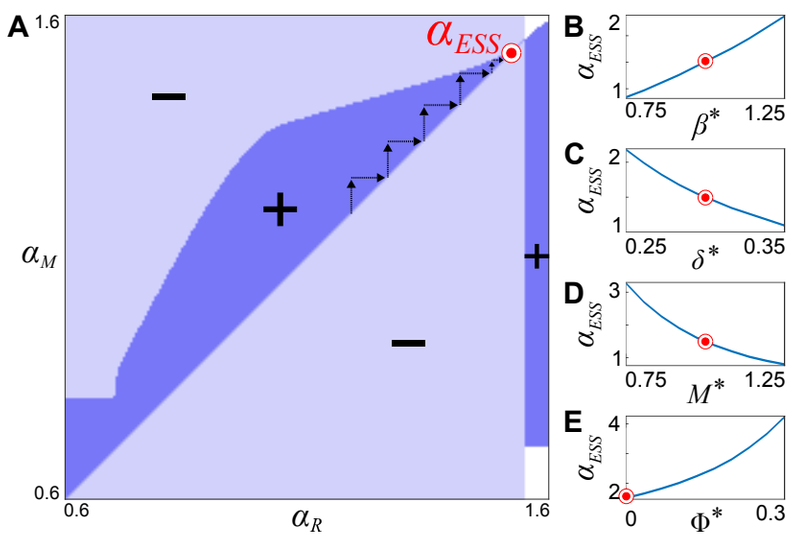

Fig. 4. A game theoretical analysis of the coupled biofilm model predicts an evolutionary stable growth rate. (A) We used adaptive dynamics to construct a pairwise invasion plot, which maps the region of parameter space where a mutant, which grows at rate α_M, can invade a resident population of biofilms, which grow at rate α_R (see text). The mutant can invade in the dark blue regions (+) and cannot invade in the light blue regions (−). In the white regions the mutant and the resident biofilms both have a fitness of zero ($W_i = 0$) because they have either been fully detached by flow, or have blocked their pore space. Arrows show an example evolutionary trajectory where mutant genotypes successively replace the resident population, driving the growth rate towards the evolutionary stable growth rate, α_{ESS} (red circle). Here we set $\delta^* = 0.3\alpha_R^{-1/2}$ and $\beta^* = 1.1\alpha_R^{-1}$, $M^* = 1$, and $\Phi^* = 0$. (B, C, D, E) To determine the effect of β^*, δ^*, M^*, and Φ^* on α_{ESS}, we held three of these parameters constant and varied the fourth (red circles show fixed values).

1 Supporting Information

1.1 Control Experiments

We performed separate experiments to ascertain if the dye used in the competition experiments or the different fluorescent markers had an effect on biofilm development. We injected cells into straight microfluidic channels (1 mm width, 75 μm depth) and then clamped the tubing on either side of the channel to allow cells to attach in the absence of flow for 60 mins. We then started an injection of tryptone broth (0.5 x TB, 5 g Tryptone per liter of water, with or without dye) at a flow rate of 0.1 ml h^{-1} and imaged the biofilm within each of the channels every 30 minutes for 78 hours. These microfluidic devices were fabricated and plumbed using the same techniques described in the *Materials and Methods*. In these experiments we used 60 ml syringes mounted on a Harvard Apparatus PhD Ultra syringe pump. To minimize flow induced detachment, and thus more accurately measure biofilm growth, these experiments used relatively small shear stresses. Here the shear stress at the beginning of the experiment was τ=0.030 kg m^{-1} s^{-2}, >150 times smaller than in the beginning of the high flow rate treatment in the competition experiment and >7 times smaller than that in the beginning of the low flow treatment. See section below for calculation of shear stresses.

1.2 Microscopy and image processing

We imaged microfluidic experiments using a Zeiss Axio Observer inverted microscope with an AxioCam MRm camera, and a Definite Focus system. A Zeiss Plan Apochromat 20X objective was used for competition experiments (Fig. 2), whilst a Zeiss EC Plan Neofluar 10X objective was used for control experiments (Fig. S2). We used the software package Zen Blue (Zeiss) to automatically record brightfield, GFP, and RFP images at each time point. As our devices were larger than a single field of view we recorded multiple adjacent images and stitched them together in post processing. To clarify the presentation of Fig. 2 *A,B*, we plotted each strain's fluorescence only in the arm of the device in which it was localized, so that the dye interface was more visible downstream.

To quantify the proportion of flow moving through each arm of the competition device over time, we manually tracked the location of the dye interface using the image analysis software Fiji [94] and applied a moving average filter to reduce sampling noise (Fig. 2 *A,B,C*). This analysis neglects the thickness of the biofilm growing in the downstream channel of the device, which acts to further reduce the thickness of the dye stream, h_D (Fig. 2 *A, B*). A similar technique was used to enumerate the thicknesses of the biofilms over time (Fig. 2 *D,E*). We measured the thickness of each genotype in three different positions along the device upstream of the junction. The time series of biofilm thickness at each point was smoothed to reduce sampling noise: the mean and standard deviation of these are plotted in Fig. 2 *D,E*.

1.3 Using a hydrodynamic model to resolve how flow distributes in competition experiments

Here we develop a physical model to convert measurements of the position of the dye interface, h_D/H_D (see Fig. S1B), into the volumetric flow rates passing through the arms of the device occupied by the wildtype and rpoS null biofilms, denoted by q_1 and q_2 respectively. Conservation requires $Q_T = q_1 + q_2$, where Q_T is the total volumetric flow rate externally imposed by the syringe pump. At the end of the low flow rate experiment, the wild type biofilm gradually reduces its access to flow, causing h_D/H_D to become progressively smaller until the dye interface can no longer be discerned. However, we still expect that that $q_1 > 0$ when this occurs, because the wild type biofilm has not grown thick enough to fully block its porespace i.e. $2(L-k) > 0$ (see Figure 2A,D). Therefore, a key question is: What is the smallest flow that can be resolved with the dye interface?

In the absence of molecular diffusion of dye, the interface would remain sharp and precisely track the streamline that forms the boundary between two fluid streams coming from either inlet. In this limit we

could measure the flow past the wild-type biofilm, even as it becomes arbitrarily small. In reality, however, molecular diffusion of the dye causes a gradient of dye to form in the direction traverse to flow, causing the dye interface to become more diffuse as one moves further downstream from where the two streams meet one another. The width of the dye gradient is quantified by the diffusive lengthscale, L_G, which is measured in the direction traverse to flow. This is given by

$$L_G = \sqrt{\frac{2DZ_D}{U}},$$

where $D = 700\ \mu\text{m}^2\ \text{s}^{-1}$ is the diffusion coefficient of Chicago Blue dye [98], $Z_D = 100\ \mu$m is the distance down the channel to where the dye interface is measured (Figs. 2 and S1), and U is the mean speed of the flow along the dye interface.

Molecular diffusion of the dye thus places a key limitation on the smallest q_1 that can detected in our experiments. More specifically once, h_D, the width of the stream of the dyed media becomes comparable to the width of the dye gradient, L_G, the position of the dye interface can no longer be discerned. Here develop a mathematical model to predict the magnitude of q_1 when $h_D \approx L_G$, and thus estimate the smallest flow past the wild type biofilm that we can resolve.

Assuming pressure driven Poiseuille flow through a channel of square cross section, the volumetric flow rate can be obtained by integrating the velocity profile $u(x, y)$. For a channel of cross section A,

$$q_T = \int_A dx\ dy\ u(x, y). \tag{13}$$

Using the geometry presented in Fig. S1B, $H_D = 2H$, and $\phi = H/B$, we rescale via

$$x = BX, \quad y = By, \quad u(x, y) = [-B^2 dP/\mu]\psi(X, Y),$$

where dP is the change in pressure per unit length of the channel and ψ is the rescaled velocity, such that

$$q_T = \frac{B^4 dP}{\mu} g_1(\phi), \qquad g_1(\phi) := \left(-\int_{-\phi}^{\phi} dX \int_{-1}^{1} dY \psi(X, Y) \right). \tag{14}$$

One has, from conservation of momentum in the z direction,

$$\psi_{XX} + \psi_{YY} = 1, \quad X \in [-\phi, \phi], \quad Y \in [-1, 1],$$

where subscripts denote partial derivatives and $\psi = 0$ on all boundaries. This formulation allows solution by separation of variables as detailed in [91]. By mapping between the notation used here and that in[91], and with $\lambda_m := (2m + 1)\pi/2$, one has

$$\psi(X, Y) = \frac{1}{2}(Y^2 - 1) + \sum_{m=0}^{\infty} \frac{2(-1)^m}{\lambda_m^3} \cos(\lambda_m Y) \tanh(\lambda_m X).$$

Hence

$$g_1(\phi) = \frac{4\phi}{3} - 8 \sum_{m=0}^{\infty} \frac{\tanh(\lambda_m \phi)}{\lambda_m^5}$$

and

$$q_T = \frac{B^4 dP}{\mu} g_1(\phi) = \frac{4HB^3 dP}{3\mu} \left(1 - \frac{1}{6} \frac{B}{H} \sum_{m=0}^{\infty} \frac{\tanh(\lambda_m \phi)}{\lambda_m^5} \right).$$

The mean fluid velocity along the dye interface can be calculated as:

$$U = \frac{1}{2L} \int_{-B}^{B} dy\ u(-H + h_D, y) = -\frac{B^2 dP}{2\mu} \int_{-1}^{1} dY \psi(-\phi + h_D/B, Y) =: \frac{B^2 dP}{2\mu} S_2 \left(\frac{h_D}{B}, \phi \right), \tag{15}$$

which defines the function S_2, which is positive. Integrating the separation of variables solution for ψ gives

$$S_2(h_D/B,\phi) = \frac{2}{3} - 4\sum_{m=0}^{\infty} \frac{\cosh(\lambda_m(-\phi + h_D/B))}{\cosh(\lambda_m\phi)\lambda_m^4}, \quad \lambda_m := \frac{\pi}{2}(1+2m).$$

Thus

$$L_G^2 = \frac{4\mu D Z_D}{B^2 dP S_2(h_D/L,\phi)},$$

and, using equation (14), ${h_D}^2 \gg L_G^2$ is equivalent to

$$S_2(h_D/B,\phi)\frac{{h_D}^2}{B^2} \gg S_2(h_D/B,\phi)\frac{L_G^2}{B^2} = S_2(h_D/B,\phi)\frac{4\mu D Z_D}{B^4\ dP\ S_2(h_D/B,\phi)} = \frac{4DZ_D}{q_T}g_1(\phi). \tag{16}$$

Here we consider our slow flow rate experiments where $Q_T = 0.1$ cm^3 hr^{-1} and estimate the flow rate q_1 through wild type biofilm's pore space as it begins to block. The dye interface is measured in the downstream section of the channel (Fig. 2A) where $\phi = 2H/2B = 150\ \mu m\ /\ 75\ \mu m = 2$.

The dye interface will not be altered significantly (i.e. to leading order of magnitude) by the influence of diffusion provided $h_D > \sqrt{10}L_G$. Diffusion is no longer negligible once $h_d \approx \sqrt{10}L_G$, whereby

$$S_2\left(\frac{h_D}{B},\phi\right)\frac{{h_D}^2}{B^2} \approx 10\frac{4DZ_D}{q_T}g_1(2)$$

and this expression can be evaluated to yield $h_D/B \approx 0.5$, or equivalently $h_D/H_D \approx 0.125$, where H_D is the channel width and $H_D = 2H = 2\phi B = 4B$. Similarly, we can predict when the position of the dye interface can no longer be detected. This occurs when h_D and L_G become comparable to one another. This occurs when:

$$S_2\left(\frac{h_D}{B},\phi\right)\frac{h_D^2}{B^2} \approx \frac{4DZ_D}{q_T}g_1(2)$$

and this expression yields $h_D/L \approx 0.215$, or equivalently $h_D/H_D \approx 0.05$. These calculations are in agreement with our experimental observations, where we measure $h_D/H_D = 0.07$ at $t = 38$ h, but the dye interface is no longer visible at the measurement location by $t = 39$ h (Fig. 2).

The fraction of flow through the wildtype biofilm's porespace q_1 can now be related to h_D/H, and thus h/H_D very easily. We have:

$$q_1 = \int_{-H}^{-H+h_D} dx \int_{-B}^{B} dy\ u(x,y) = -\frac{B^4\ dP}{\mu}\int_{-\phi}^{-\phi+h_D/B} dX \int_{-1}^{1} dY \psi(X,Y) \tag{17}$$

$$= \frac{B^4\ dP}{\mu}\int_{-\phi}^{-\phi+h_D/B} dX S_2(\phi+X,\phi) = \frac{B^4 dP}{\mu}\int_0^{h_D/B} d\zeta S_2(\zeta,\phi) \tag{18}$$

using the definition of S_2 above. For $\phi = 2$, we have

$$\frac{q_1}{q_T} = \frac{B^4 dP}{\mu q_T}\int_0^{h_D/B} d\zeta S_2(\zeta,2) = \frac{1}{g_1(2)}\int_0^{h_D/B} d\zeta S_2(\zeta,2) \approx 0.5466\int_0^{h_D/B} d\zeta S_2(\zeta,2).$$

This can be determined by using the above expression for S_2. By curve fitting the numerically calculated q_1/Q_T for $\phi = 2$ one finds, for $h_D \le H$,

$$\frac{q_1}{q_T} \approx \frac{1}{2}\left(\frac{h_D}{H}\right)^{3/2} = \sqrt{2}\left(\frac{h_D}{H_D}\right)^{3/2},$$

which provides a more convenient expression. Our analysis thus predicts that our measurement of the dye interface only begins to be affected by molecular diffusion when $q_1/Q_T \approx 0.06$ (when $h_D/H_D \approx 0.125$) and the loss of the dye interfaces is only assured when $q_1/Q_T \approx 0.02$ (when $h_D/H_D \approx 0.05$). Therefore, the dye interface can be used to reliably measure the flow along the wild type biofilm's flow path until it has decreased to just a few percent of the total flow rate.

1.4 Inferring the rates of biofilm dispersal in competition experiments using empirical measurements

To estimate how the sloughing rate, W, of either biofilm changes over time, we combine results from the previous section with direct measurements of biofilm thickness to determine the hydrodynamic shear stress acting on the surface of the biofilm, τ. The time series of τ can then be used in the parameterization of Rittman [50] to directly infer the rate at which the biofilm sloughs from the surface. The dispersal rate is given by $W = \chi k_i \tau^{1/2}$, which is also used in our Eqn. 1. This parameterization is widely used in the literature and has been independently verified in porous environments ([45, 51, 52, 53, 54, 55] and see main text).

In this analysis, we cannot directly compare the dispersal rates between the genotypes because a biofilm's intrinsic propensity to detach, χ, could potentially vary between our genotypes [62]. Instead, we calculate how the dispersal rate of each biofilm changes over time [50] to shed light on what happens to dispersal as the wild type biofilm blocks its flow supply. Consider the channel occupied by the wild type biofilm, whose cross section has dimensions $2B = 75$ μm and $2L = 65$ μm (Fig S1B), and has a biofilm of thickness k_1 growing on all four surfaces. Using the result presented in the following section, titled "Estimation of the shear stresses in rectangular channels" we have the average shear stress on the face of the wild type channel of length $2B$ is given by

$$\tau_B = \frac{3\mu q_1}{4b_1\ell_1^2} f\left(\frac{\ell_1}{b_1}\right),$$

where $b_1 = B - k_1$ and $\ell_1 = L - k_1$. Here, $f(\phi) \approx 1 + 0.06827\phi + 0.1173\phi^2$ (see following section) and has relative errors bounded by 10^{-1} for $\phi \in [0, 3]$. Using symmetry, or explicit calculation, the average shear stress on the face of the wild type channel of length $2L$ is given by

$$\tau_L = \frac{3\mu q_1}{4b_1^2\ell_1} f\left(\frac{b_1}{\ell_1}\right)$$

and relative accuracy of 10% or better is maintained in the expression for $f(\phi)$ provided that $k_1 \leq 30$ μm, which corresponds to a channel where the biofilm has nearly almost fully grown across the channel (a channel which has fully blocked corresponds to $k_1 = L = 65/2$ μm).

To determine the dispersal per unit length along the channel occupied by the wild type biofilm, we add the dispersal per unit area along each face, weighted by the length of the face:

$$W_1 = \chi_1 k_1 \left(4b_1\tau_B^{1/2} + 4\ell_1\tau_L^{1/2}\right),$$

where χ_1 is the dispersion parameter of the wild type biofilm (see main text). With the approximation of the previous section, $q_1 = Q_T\sqrt{2}\left(h_D/H_D\right)^{3/2}$, we have

$$W_1 = 2\sqrt{3\mu}\chi\left[\sqrt{2}Q_T\left(\frac{h_D}{H_D}\right)^{3/2}\right]^{1/2} k_1 F(b_1, \ell_1),$$

and analogously, the dispersal rate per unit length along the $\Delta rpoS$ biofilm's channel is given by

$$W_2 = 2\sqrt{3\mu}\chi_2\left[Q_T - \sqrt{2}Q_T\left(\frac{h_D}{H_D}\right)^{3/2}\right]^{1/2} k_2 F(b_2, \ell_2),$$

where

$$F(b_i, \ell_i) = \left[\frac{b_i}{\ell_i^2}\, f\left(\frac{\ell_i}{b_i}\right)\right]^{1/2} + \left[\frac{\ell_i}{b_i^2}\, f\left(\frac{b_i}{\ell_i}\right)\right]^{1/2},$$

$b_2 = B - k_2$, $\ell_2 = L - k_2$, and χ_2 is the dispersion parameter of the $\Delta rpoS$ biofilm. Because μ, χ_1 and χ_2 do not change over the course of an experiment, we define the normalized dispersion rates

$$W_1' = \frac{W_1}{2\sqrt{3\mu}\chi_1} = \left[\sqrt{2}Q_T\left(\frac{h_D}{H_D}\right)^{3/2}\right]^{1/2} k_1 F(b_1, \ell_1),$$

and

$$W_2' = \frac{W_2}{2\sqrt{3\mu}\chi_2} = \left[Q_T - \sqrt{2}Q_T\left(\frac{h_D}{H_D}\right)^{3/2}\right]^{1/2} k_2 F(b_2, \ell_2).$$

to estimate how the dispersal rate changes over time without direct empirical measurement of the constants χ_1, χ_2.

The normalized dispersal rates are plotted in Fig. S6 for both flow treatments. This analysis indicates that the wild-type biofilm sharply reduces its dispersal rate in the low flow rate treatment experiment, whilst the rpos mutant sharply increases its dispersal rate. In contrast, in the high flow rate experiment, the both genotypes initially increase their dispersal rate, but then begin to plateau. These results resemble regimes f and b in our numerical model of biofilm formation (Figure 3). While technical limitations prohibit direct measurement of the dispersal rates in our experiments, these analyses strongly support our assertion that rapidly growing biofilms can limit their dispersal by reducing their access to flow.

1.5 Estimation of the shear stresses in rectangular channels

The mean shear stresses within our microfluidic devices can be derived from the equations for Poiseuille flow through a rectangular channel [91]. For a channel of width $2L$ and depth $2B$, where $L \leq B$, the mean shear stress on the side of length $2B$ is given by

$$\tau = \frac{3q\mu}{4BL^2} f(\phi), \tag{19}$$

where μ is the dynamic viscosity of the media, q is the volumetric flow rate through the channel, and $f(\phi)$ is solely a function of the aspect ratio $\phi = L/B$. The function $f(\phi)$ can be determined by using separation of variables to solve the governing non-dimensional equations [91]. The resulting expression is complicated so here we provide more compact quadratic interpolation for $f(\phi)$

$$f(\phi) \approx 1 + 0.06827\phi + 0.1173\phi^2, \tag{20}$$

where relative errors are no more than 10^{-3} for $L \leq B$.

For the competition channels (Fig. 2), this expression yields a mean shear stress $\tau = 0.23$ kg m^{-1} s^{-2} for the low flow rate treatment and $\tau = 4.7$ kg m^{-1} s^{-2} for the high flow rate treatment condition. In the control experiment (Fig. S2) $\phi = 0.075$ yielding a mean shear stress of $\tau = 0.030$ kg m^{-1} s^{-2}. These calculations estimate the shear stresses at the beginning of the experiments when the thickness of the biofilm is negligible and the flow through the two arms of the device are equally balanced. We assumed $\mu = 1.0$ mPa s, the standard value for the viscosity of water at 20°C.

1.6 Extensions to incorporate dependencies between growth rate and dispersal

Our initial model assumes that both competing genotypes can equally resist detachment; however, previous studies have shown the rate of detachment can depend on both the flow environment and the biofilm's growth rate [62, 63]. To capture this additional dependency we extended our model to take into account growth rate dependent detachment, using an empirically derived formulation first proposed by Speitel and DiGiano (1987), who examined biofilms growing under different nutrient conditions. This adds an additional term to our model where detachment is proportional to the biofilm growth rate. The new model reads,

$$\frac{dk_1}{dt} = \alpha_1 \min(\delta_1, k_1) - k_1\sqrt{\tfrac{3\mu Q_T \chi^2}{4B}}\sqrt{\tfrac{(L-k_1)}{(L-k_1)^3+(L-k_2)^3+M^3}} - \Phi^* \alpha_1 \min(\delta_1, k_1), \tag{21}$$

$$\frac{dk_2}{dt} = \alpha_2 \min(\delta_2, k_2) - k_2\sqrt{\tfrac{3\mu Q_T \chi^2}{4B}}\sqrt{\tfrac{(L-k_2)}{(L-k_1)^3+(L-k_2)^3+M^3}} - \Phi^* \alpha_2 \min(\delta_2, k_2). \tag{22}$$

Here, as in Speitel and DiGiano, Φ^* is a dimensionless parameter measuring the strength of this dependency ($0 \leq \Phi < 1$). Non-dimensionalizing as in the main text then yields,

$$\frac{dk_1}{dt} = \min(k_1, \delta^*) - \beta^* k_1 \sqrt{\frac{(1-k_1)}{\theta}} - \Phi^* \min(\delta^*, k_1), \tag{23}$$

$$\frac{dk_2}{dt} = \alpha^* \min(k_2, \frac{\delta^*}{\sqrt{\alpha^*}}) - \beta^* k_2 \sqrt{\frac{(1-k_2)}{\theta}} - \Phi^* \alpha^* \min(k_2, \frac{\delta^*}{\sqrt{\alpha^*}}), \tag{24}$$

$$\text{where } \theta = (1-k_1)^3 + (1-k_2)^3 + (M^*)^3. \tag{25}$$

As above, these were solved numerically using Matlab until each biofilm had converged to a steady state thickness. More generally, one can understand the relationship between the original model and its extension via the continuous bijection for the dimensional model

$$(\alpha_1, \alpha_2, \chi) \to (\alpha_1(1-\Phi), \alpha_2(1-\Phi), \chi). \tag{26}$$

Thus, the region of parameter space occupied by each of our competitive regimes in our initial model (Fig. 3, Eqns 8-10) will map to a non-zero volume of parameter space within the generalized model (Fig. S5, Eqns 15-17). Moreover, the boundaries between each of these regimes map continuously, meaning the structure of the parameter space of the initial model will be preserved in the generalized model (Fig. S5). In other words, adding the additional dependency between growth and detachment will not eliminate or nor add additional regimes of competition, nor affect position of the competitive regimes relative to one another within the $[\alpha^*, \beta^*]$ parameter space.

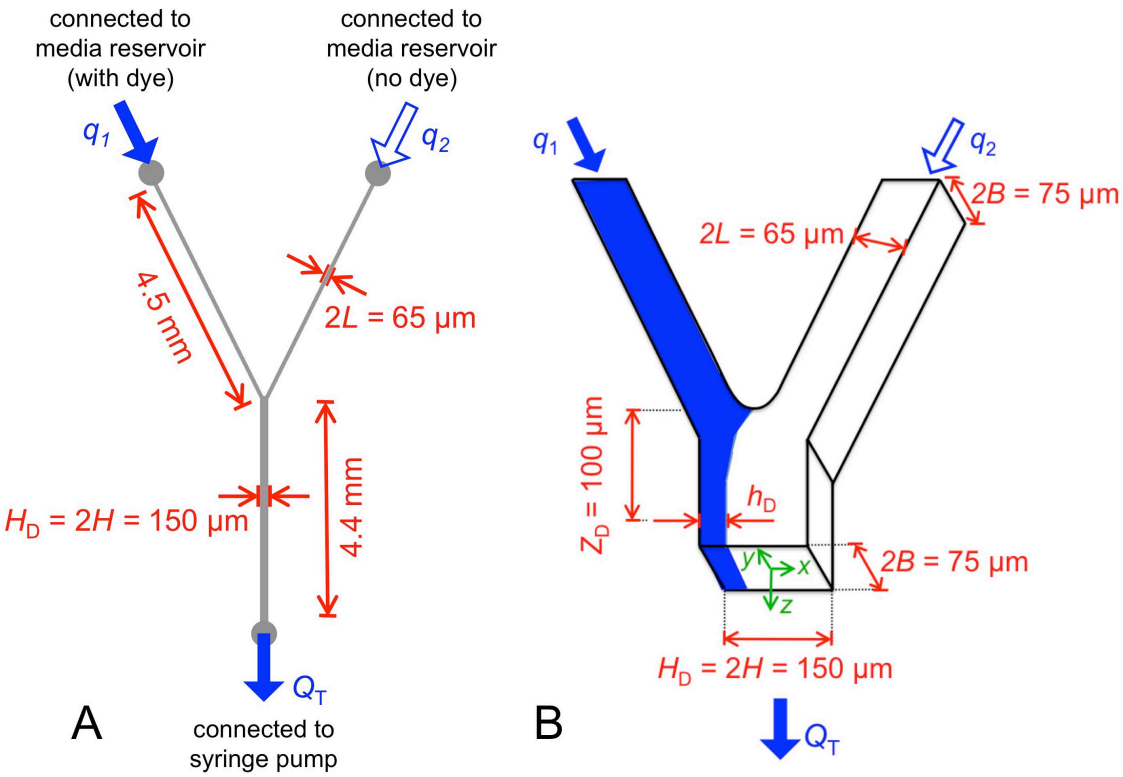

Figure S1: **Schematic of microfluidic device that simulates the hydrodynamic interactions between patches of biofilm within a porous environment.** (A) A syringe pump was used to pull fluid through the bottom outlet of the device at a constant volumetric flow rate, Q_T, whilst the upper inlets of the device were connected to either a reservoir of media containing dye or a reservoir without dye (*Materials and Methods*). While the total flow through the system is fixed at $Q_T = q_1 + q_2$, the proportion of flow passing through each of the two upper arms is determined by their relative hydrodynamic resistances, which are in turn a function of the thicknesses of the biofilms that colonize each arm. (B) We dynamically track how much flow passes through each arm by measuring the location of the dye interface downstream $Z_D = 100$ μm of where the two channels meet. This allows us to track how wild-type and RpoS null biofilms, which colonize the left and right hand arms of the device respectively, affect one another's access to flow (Fig. 2). As Q_T is held constant, biofilm growth downstream of the junction does not affect the proportion of flow passing through each of the upstream arms.

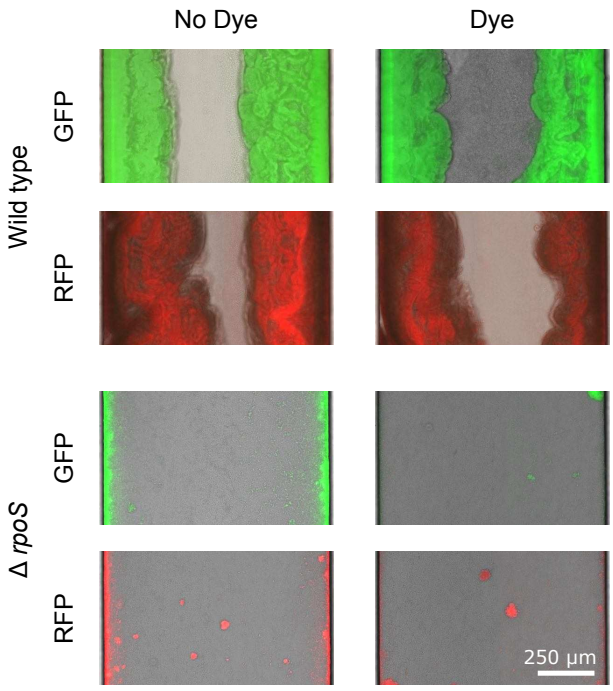

Figure S2: **Wild type biofilms form at a faster rate than RpoS null biofilms.** We inoculated relatively wide straight microfluidic channels ($2B = 1$ mm by $2L = 75$ μm cross section) with either WT or Δ*rpoS* cells (*Materials and Methods*) and tracked biofilm formation over 96 hours. The wild type cells always formed much thicker biofilms than the mutant. These controls show that neither the fluorescent protein (RFP, GFP) nor the Chicago Blue dye was responsible for this difference.

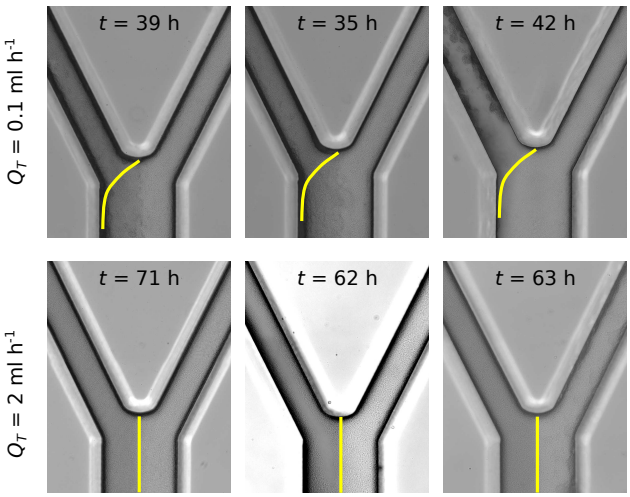

Figure S3: **Three independent repeats of our competition experiment yielded the same result at steady state.** In the low flow treatment (Q_T = 0.1 ml h^{-1}), the WT biofilm, which colonized the left arm, consistently blocked its porespace. In contrast, in the high flow rate treatment (Q_T = 2 ml h^{-1}) both genotypes were able to retain access to flow. Stochastic variation in initial cell attachment likely was responsible for the variation in the timescale of blocking. The first column shows the experiments shown in Fig. 2.

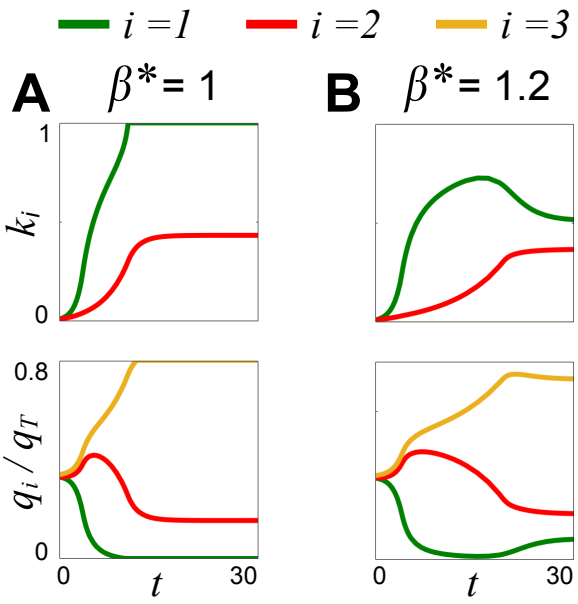

Figure S4: **The impact of flow on biofilm competition**. As a biofilm grows it increases the hydrodynamic resistance of its pore space, which tends to decrease both its access to flow (Fig. 1) and flow-induced detachment. This creates a positive feedback loop because decreased detachment further increases its hydrodynamic resistance. When flow is weak (A) this process can lead to the faster growing genotype (green, $i = 1$) completely blocking its pore space, such that it can no longer disperse cells downstream (Fig. 3 f). However, when flow is stronger (B), increased detachment prevents the faster growing biofilm from blocking, but as the slower growing biofilm (red, $i = 2$) increases in thickness it diverts flow back to the faster growing biofilm, which then reduces in thickness. Here $M^* = 1, \delta^* = 0.3, \alpha^* = 1.5$, and the yellow line indicates flow along a third flow path without biofilm ($i = 3$, Fig. 1).

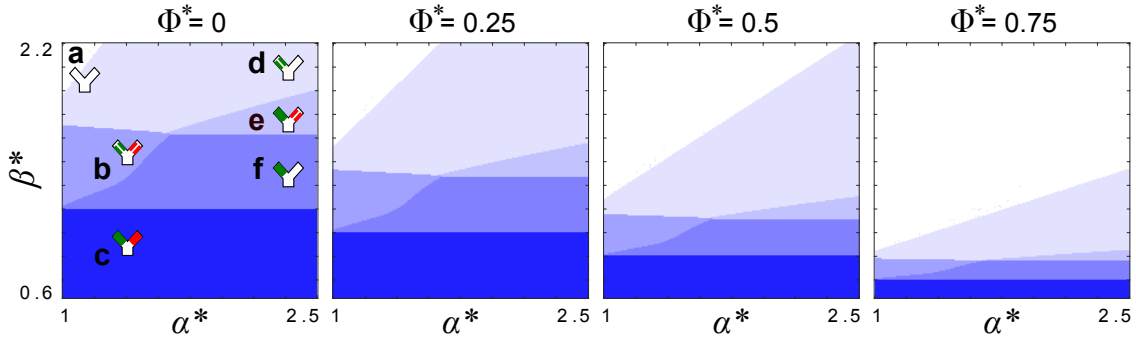

Figure S5: **A model in which a biofilm's rate of detachment is coupled to its rate of growth generates the same qualitative result as a model that omits this dependency.** While $\Phi^* = 0$ corresponds to a model where detachment and growth can vary independently, increasing Φ^* means that a biofilm's detachment rate increases more quickly with its growth rate (see text and *Supporting Information*). Inclusion of this coupling increases the parameter space where one or both genotypes are washed away, however, all of the competitive regimes, and their positions relative to one another, are conserved. This finding is consistent with theoretical predictions (see *Supporting Information*)

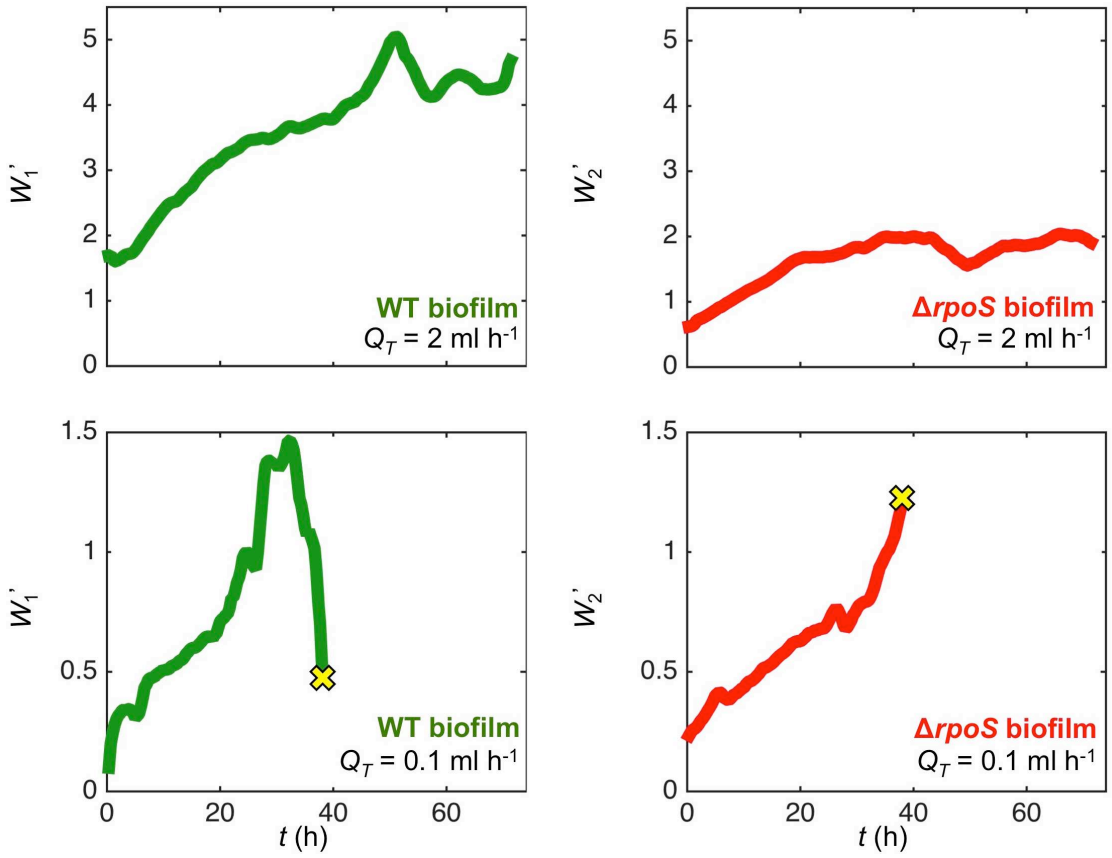

Figure S6: **Combining empirical measurements with a mechanistic model allows us to infer how the normalized biofilm dispersal rate, W_i', changes over the course of the competition experiments.** Here we use the position of the dye interface and the biofilm thickness to determine the hydrodynamic shear stress that both the wildtype and RpoS null biofilm experience over time. This information is then used as an input in an established model to estimate the rate at which cells are shed from the biofilm (see Supporting Information). This analysis finds that in the high flow rate experiment ($Q_T = 2$ ml h^{-1}), both biofilms gradually increase their dispersal rates until they begin to plateau after approximately 40 hours. In contrast, in the low flow rate experiment ($Q_T = 0.1$ ml h^{-1}) the wild type biofilm increases its dispersal rate until it begins to divert flow away (Fig. 2), which causes its dispersal rate to fall sharply. By the time that the dye interface can no longer be distinguished ($t = 38$ h, yellow crosses), the wild type biofilm's dispersal rate is only 1/3 of its peak value. In contrast, the rpoS null biofilm increases its dispersal rate over the course of the experiment. Here we plot the normalized dispersal rate of the wild type biofilm, W_1', and normalized dispersal rate of the rpoS-null biofilm, W_2'. See Supporting Information section titled "Inferring the rates of biofilm dispersal in competition experiments using empirical measurements" for details.